Effects of surface and top wind shear on the spatial organization of marine Stratocumulus-topped boundary layers

Mónica Zamora Zapata[1], Thijs Heus[2], and Jan Kleissl[3]

[1]University of California San Diego
[2]Cleveland State University
[3]University of California, San Diego

November 23, 2022

Abstract

The convective nature of Stratocumulus topped boundary layers (STBL) involves the motion of updrafts and downdrafts, driven by surface fluxes and radiative cooling, respectively. The balance between shear and buoyant forcings at the surface can determine the organization of updrafts between cellular and roll structures. We investigate the effect of varying shear at the surface and top of the STBL using LES simulations, taking DYCOMS II RF01 as a base case. We focus on spatial identification of the following features: coherent updrafts, downdrafts, and wet updrafts, and observe how they are affected by varying shear. Stronger surface shear organizes the updrafts in rolls, causes less well-mixed thermodynamic profiles, and decreases cloud fraction and LWP. Stronger top shear also decreases cloud fraction and LWP more than surface shear, by thinning the cloud from the top. Features with stronger top than surface shear are associated with a net downward momentum transport and show early signs of decoupling. Classifying updrafts and downdrafts based on their vertical span and horizontal size confirms the dominance of large objects spanning the whole STBL. Large objects occupy 14% of the volume in the STBL while smaller ones occupy less than 1%. For updraft and downdraft fluxes these large objects explain 33% of the vertical velocity variance and 53% of the buoyancy flux, on average. Stronger top shear also weakens the contribution of downdrafts to the turbulent fluxes and tilts the otherwise vertical development of updrafts.

Effects of surface and top wind shear on the spatial organization of marine Stratocumulus-topped boundary layers

Mónica Zamora Zapata [1], Thijs Heus [2], Jan Kleissl [1]

[1]Department of Mechanical and Aerospace Engineering, University of California, San Diego, La Jolla, CA, USA
[2]Department of Physics, Cleveland State University, Cleveland, OH, USA

Key Points:

- The spatial organization of Stratocumulus-topped boundary layers is sensitive to variations of surface and top wind shear.
- Strong surface and top wind shear combined reduce cloud fraction, align updrafts and clouds with the mean wind, and modify cloud top.
- Updrafts and downdrafts are identified: the largest objects dominate their composition and contribution to turbulent fluxes.

Corresponding author: Mónica Zamora Zapata, mzamoraz@eng.ucsd.edu

Abstract

The convective nature of Stratocumulus topped boundary layers (STBL) involves the motion of updrafts and downdrafts, driven by surface fluxes and radiative cooling, respectively. The balance between shear and buoyant forcings at the surface can determine the organization of updrafts between cellular and roll structures. We investigate the effect of varying shear at the surface and top of the STBL using LES simulations, taking DYCOMS II RF01 as a base case. We focus on spatial identification of the following features: coherent updrafts, downdrafts, and wet updrafts, and observe how they are affected by varying shear. Stronger surface shear organizes the updrafts in rolls, causes less well-mixed thermodynamic profiles, and decreases cloud fraction and LWP. Stronger top shear also decreases cloud fraction and LWP more than surface shear, by thinning the cloud from the top. Features with stronger top than surface shear are associated with a net downward momentum transport and show early signs of decoupling. Classifying updrafts and downdrafts based on their vertical span and horizontal size confirms the dominance of large objects spanning the whole STBL. Large objects occupy 14% of the volume in the STBL while smaller ones occupy less than 1%. For updraft and downdraft fluxes these large objects explain 33% of the vertical velocity variance and 53% of the buoyancy flux, on average. Stronger top shear also weakens the contribution of downdrafts to the turbulent fluxes and tilts the otherwise vertical development of updrafts.

Plain Language Summary

Stratocumulus clouds form in the atmospheric boundary layer, close to the Earth's surface. Turbulence in this boundary layer causes large circulation composed of strong motions going up and down called updrafts and downdrafts. At the surface and top of the boundary layer, wind speed can change abruptly, generating wind shear. We investigate the effect of changes in wind shear on the organization of the clouds, updrafts, and downdrafts. By simulating atmospheric flow, we observe that stronger surface wind reduces the amount of clouds, strong top shear modifies the shape of cloud tops, and only when shear is strong both at the surface and top, clouds are elongated in the wind direction. Of all the updrafts and downdrafts found, the largest ones dominate in volume occupied and in the transport of momentum, heat, and moisture in the boundary layer.

1 Introduction

Stratocumulus (Sc) clouds cover 23 percent of the Earth's ocean surface (Wood, 2012) and are important for the global climate because of their high albedo (Zelinka et al., 2017), as well as for solar power generation due to their presence over coastal land (Clemesha et al., 2017). Both the albedo and solar variability are directly linked to the spatial organization of the cloud field. At large scales (tenths of kilometers), mesoscale shallow convection organizes in rolls, open cells, and closed cells with different cloud fractions (Atkinson & Zhang, 1996), while at smaller scales, boundary layer processes can also impact the physics and organization of Sc.

The Stratocumulus Topped Boundary Layer (STBL) forcings act at both the surface and the BL top and determine the temporal and spatial evolution of the cloud layer. The balance between surface buoyancy flux and surface wind shear affects the turbulence and organization within the STBL. In shear-dominated convective boundary layers (CBL) streaky structures develop near the surface, in buoyancy-dominated CBLs coherent updrafts form near the surface and transport momentum throughout the CBL (Salesky et al., 2017); when both shear and buoyancy are important, coherent updraft rolls develop in the lower half of a STBL (Moeng & Sullivan, 1994) and – in the case of shallow cumulus clouds – lead to a increased cloud fraction (Park et al., 2017).

Near the top of the STBL, radiative cooling promotes a sharp temperature inversion, and there is entrainment of air from the free troposphere, and wind shear across the interface. The top of the STBL represents a sheared stratified layer with updrafts and downdrafts underneath. Radiative cooling is believed to drive downdrafts in the STBL (Wood, 2012), although recent studies question that causal relationship (Matheou & Teixeira, 2019). Wind shear across the inversion can dilute the cloud top by enhancing turbulent mixing (McMichael et al., 2019; Kopec et al., 2016; Mellado et al., 2014; Wang et al., 2012, 2008), caused by the development of Kelvin-Helmholtz waves (Wang et al., 2012; Kim et al., 2003).

The main coherent structures in STBLs are updrafts and downdrafts, and their organization is tightly linked to the turbulence and spatial features of the cloud field. The strong mixing by updrafts and downdrafts promotes the well-mixed profiles that are characteristic of STBLs (Lilly, 1968). Their importance in non-local mixing has led to the development of mass flux parameterizations with consideration of downdrafts to improve turbulent parameterizations in NWP models (Han & Bretherton, 2019; Wu et al., 2020). Recent studies have focused more closely on the identification of updrafts and downdrafts in the STBL (Davini et al., 2017; Chinita et al., 2018; Brient et al., 2019), finding that these structures are responsible for nearly 80% of the heat and moisture fluxes in the STBL (Brient et al., 2019). Another recent study has found that the horizontal scales of STBL convection tend to grow in time, a phenomenon that is enhanced by spatial perturbations of radiative cooling, i.e. more variability of cloudiness (Zhou & Bretherton, 2019). A better understanding of the dynamics and sensitivity of these structures to physical processes could further improve turbulence parameterizations tailored for STBLs.

In summary, surface and top conditions cause spatial differences in the organization of Sc clouds as well as of updrafts and downdrafts. The literature survey above reveals several open research questions: (i) For surface shear, it is unknown if the development of rolls increases Sc cloud fraction, as is the case for shallow cumulus clouds. (ii) For top shear, it is unknown if the decreased cloud fraction has an impact on STBL spatial features and if gravity waves affect the cloud field. (iii) While it is known that updrafts and downdrafts can change their structure from cells to rolls with increasing surface shear (Moeng & Sullivan, 1994), we do not know how their contribution to the turbulent fluxes in the STBL is affected by the relative magnitudes of surface and top shear, and how their contribution depends on the size of the structures.

In this work, we study the effects of varying the surface and top wind shear on the spatial structure of STBLs, which touches on all three open questions mentioned above. Using LES, we analyze the differences in cloud fraction and cloud shape, the changes in the organization of coherent structures, and their contributions to the turbulent fluxes of the STBL. Section 2 describes the LES simulations, the method to identify the coherent structures, and the geometric classification of coherent structures based on size and location. Section 3 present the results and discussion, including the effect of wind shear on the thermodynamic profiles and turbulent fluxes (Section 3a), the spatial organization of the cloud fields and structures (Section 3b), and the contributions of the classes of coherent structures on the total turbulent fluxes in the STBL (Section 3c). Section 4 contains the conclusions.

2 Methods

2.1 Simulation setup

We vary the surface and top wind speed profiles to create combined variations of shear around a reference case. The first research flight of the DYCOMS II field campaign (RF01, Stevens et al. (2005)) is the reference case for our simulations, since it is a Sc case that has been extensively studied.

To control the influence of the surface wind shear, we consider five progressions of the initial wind profile in the STBL (u_0, v_0) from the reference RF01 case (CTRL) to a case with zero mean wind speed (000U). All of these cases have no wind shear at the top of the STBL. To minimize the development of top shear during the simulation (as remarked by Fedorovich and Conzemius (2008), who argued that it can artificially enhance entrainment in LES), we nudge the wind velocity field in the whole domain with a timescale of 0.5 h. Nudging, also known as Newtonian relaxation, adds a term to the horizontal flow component equations (u and v), with the goal of enforcing the mean wind speed to follow the reference values. For u, the nudging term is

$$\left(\frac{\partial u}{\partial t}\right)_{\text{nudge}} = \frac{u_0 - u}{\tau} \tag{1}$$

where u_0 is the reference initial wind speed component and τ is the nudging timescale. The wind speed magnitude $r(z) = \sqrt{u^2 + v^2}$ in Fig. 1-a confirms that the top shear for these cases is minimal.

We also vary the wind shear at the top of the STBL in the following three base cases: the reference case (CTRL) and the cases with half (050U) and no wind speed (000U). We impose an initial top shear of $|\Delta r| = \{5, 10\}$ m s^{-1} (denoted as cases S5 and S10, respectively), where $\Delta r = r_{\text{FT}} - r$ is the jump between the tropospheric and STBL wind speed magnitudes. No nudging is imposed on the top-wind sheared cases. The values of $|\Delta r| = \{5, 10\}$ m s^{-1} agree with the referential wind speed shear reviewed by Wang et al. (2012) from VOCALS-REx. Refer to Table S1 in the supporting information for further details on the initial wind profile.

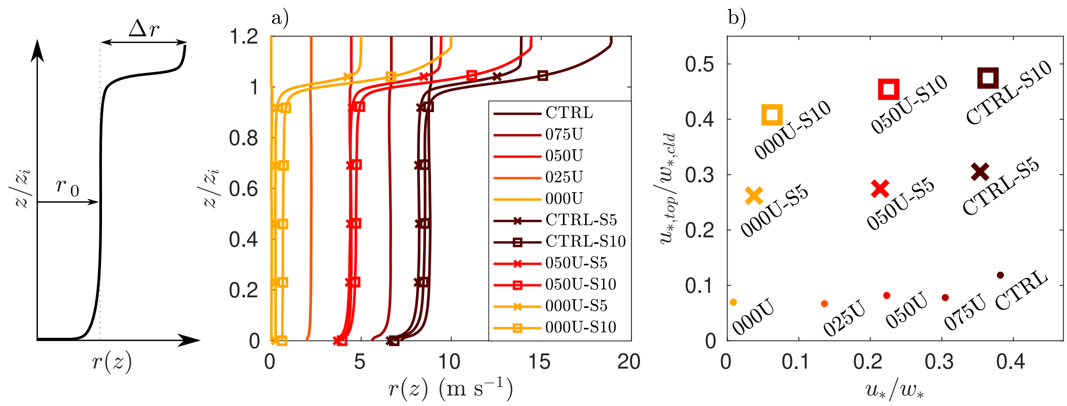

Figure 1. Wind speed variations for all the cases considered: (a) profiles of wind speed magnitude $r(z)$, and (b) case description in the parameter space defined by non dimensional measures of surface shear (u_*/w_*) and top shear ($u_{*,\text{top}}/w_{*,\text{cld}}$). Values presented are 15 minute averages at hour 4.

The flow is resolved using the UCLA-LES code following the setup by Stevens et al. (2005) in a larger domain size of 14 km × 14 km to allow for the development of stronger updraft and downdraft motions (Pedersen et al., 2016). We use a horizontal resolution of $\Delta x = \Delta y = 35$ m and a vertical resolution of $\Delta z = 10$ m in the lower part of the STBL, reduced to a minimum $\Delta z = 5$ m near the STBL top, with a total of 400×400×131 points. Surface fluxes are fixed throughout the simulation, with SHF = 15 W m^{-2} and LHF = 115 W m^{-2}.

2.2 A parameter space for wind shear variations

Previous studies have shown that the organization of the updrafts in the STBL depends on the balance between surface shear and buoyancy, and more precisely on the stability parameter $\eta = -z_i/L_{\mathrm{ob}}$, where z_i is the height of the STBL (defined here as the height of the maximum gradient of liquid water potential temperature, θ_l), and L_{ob} is the Obhukov length,

$$L_{\mathrm{ob}} = \frac{-z_i}{\kappa}\left(\frac{u_*}{w_*}\right)^3, \tag{2}$$

where κ is the von Kármán constant, u_* is the friction velocity, and w_* is the convective velocity scale: $w_* = gz_i\overline{w'\theta'_{v0}}/\theta_{v0}$, where θ_{v0} is a reference surface virtual potential temperature, and $\overline{w'\theta'_{v0}}$ is the surface virtual potential temperature flux.

Since all cases have a similar STBL height, z_i, we can represent surface shear by measuring u_*/w_* instead of L_{ob}. In a similar fashion, we can represent top shear with appropriate shear and buoyancy scales near the top of the STBL. We choose an in-cloud buoyancy reference convective velocity (Ghonima et al., 2016),

$$w_{*,\mathrm{cld}} = \frac{g}{\theta_{v,0}}\int_{z_b}^{z_i}\overline{w'\theta'_v}dz, \tag{3}$$

and compute a top friction velocity based on the momentum flux at the top of the STBL, $u_{*,\mathrm{top}} = (\overline{u'w'}^2_{\mathrm{top}} + \overline{v'w'}^2_{\mathrm{top}})^{1/4}$. With this set of scaling parameters, the variations of surface and top shear can be presented in the parameter space defined by u_*/w_* and $u_{*,top}/w_{*,cld}$, as shown in Fig. 1b.

2.3 Structure identification and classification

Updrafts and downdrafts are loosely defined as coherent strong upward and downward motions, and previous works have used different approaches for their detection: thresholds of flow properties (Moeng & Sullivan, 1994), tracers (Brient et al., 2019; Couvreux et al., 2010), both flow properties and tracers (Davini et al., 2017; Park et al., 2016), or joint probability density functions (Chinita et al., 2018). While thresholds of flow properties will result in identifying the strongest motions in the STBL, tracers identify the strongest effective transport in the vertical direction. Both methods are sensitive to parameters choices such as thresholds or tracer timescales. Couvreux et al. (2010) compared a tracer method to a threshold method, finding differences in the points that compose each identified structure, although these differences were more expressed in the surface and top regions. The coherent structures then intrinsically depend on the detection method and their parameters (timescales and thresholds). We opt for a threshold approach due to its simplicity and because it is not clear if the tracer approach is able to capture the dynamics of decoupled STBLs, which may develop due to top wind shear (Wang et al., 2012).

We consider two different sets of structures, one related to flow properties and one that is motivated by our interest in clouds. The first set consists of updrafts and downdrafts, defined by the vertical velocity anomalies $w'(x,y,z) = w(x,y,z) - \overline{w}(z)$, where $\overline{w}(z)$ is the horizontal average of $w(x,y,z)$ at height z. The second set corresponds to moister portions of the clouds, which we will call wet updrafts. These structures are defined by the profiles of liquid water content anomalies $q'_l(x,y,z) = q_l(x,y,z) - \overline{q_l}^c(z)$, constructed with the average $\overline{q_l}^c$ using only the cloudy points (where $q_l(x,y,z) > 0$); therefore, $q'_l(x,y,z)$ is only defined for cloudy points. Even though the detection rule does not consider w, Section 3.5 will confirm that the vast majority of these structures are in fact updrafts. We choose the name “wet updrafts” instead of e.g. “cloud centers” as “wet updrafts” is more descriptive of the physical processes.

To identify coherent structures, we first apply a spatial Gaussian filter. Per Text S1 in the the supporting information, the number of objects stabilizes for larger filter radii. The chosen radii are 2 voxels for updrafts and downdrafts and 3 voxels for wet updrafts. For a generic filtered variable $\phi = \{w, q_l\}$, the points that belong to a particular structure satisfy $\phi' > \sigma_\phi(z)$ (or $\phi' \leq -\sigma_\phi(z)$ in the case of downdrafts for w), where $\sigma_\phi(z)$ is the standard deviation of ϕ at each vertical level (per Text S2 in supporting information, a reduction of 10% in the threshold results in 5% higher contributions of large updrafts and downdrafts to the vertical velocity variance). For q_l', σ_{q_l} is computed using only the cloudy points. We detect wet updrafts rather than the whole cloud because the high cloud fraction fields that are characteristic of STBL would otherwise result in only one cloud object and would not represent the spatial "texture" of the cloud field. An object is composed of the detected points that are contiguous in any direction (if either faces, edges, or corners are connected). We also account for the periodicity of the LES domain by joining objects that are adjacent at the horizontal sides of the domain.

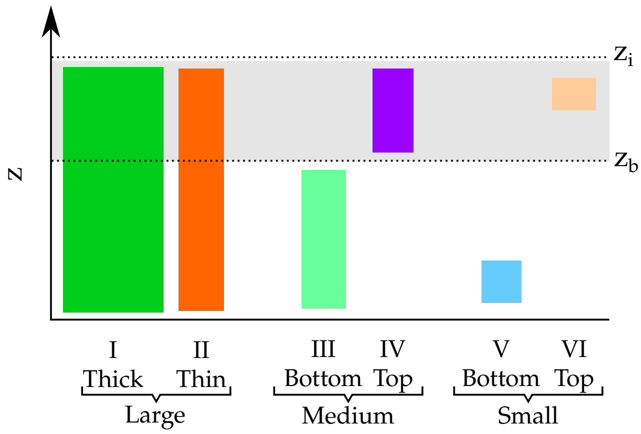

Figure 2. Visual representation of the proposed object classification. The gray area represents the cloud layer.

We classify the identified updraft and downdraft objects based on their geometrical properties as shown in Fig. 2. For each object, we compute its lowest height z_0, height span in the STBL Δz, total volume V, and an equivalent horizontal length scale $L_h = \sqrt{V/\Delta z}$. For updrafts and downdrafts, we find structures that span the whole STBL height, z_i. We also find smaller structures occupying the subcloud or cloud regions. Therefore, we classify the structures as large ($\Delta z > 0.5 z_i$), medium ($0.2 z_i < \Delta z \leq 0.5 z_i$), or small ($\Delta z \leq 0.2 z_i$). Furthermore, large structures are sub-classified by their horizontal size L_h as either thick ($L_h > \overline{L_h}$, category I) or thin structures ($L_h \leq \overline{L_h}$, category II), where $\overline{L_h}$ is the average horizontal length of the large objects. Medium and small objects are sub-classified by their position in the STBL: bottom objects occupy the subcloud region ($z_0 < z_b$, categories III and V, where z_b is the mean cloud base height) and top objects occupy the cloudy region ($z_0 \geq z_b$, categories IV and VI), where z_b is the cloud base height. In summary, we have six geometric categories for the identified objects that form updrafts and downdrafts, denoted as $\{\mathrm{UD}^{\mathrm{I}}, ..., \mathrm{UD}^{\mathrm{VI}}\}$ and $\{\mathrm{DD}^{\mathrm{I}}, ..., \mathrm{DD}^{\mathrm{VI}}\}$.

3 Results and discussion

We first describe the effects of the different shear configurations on the general properties of the STBL, and then analyze the spatial features and turbulent contributions of the updrafts, downdrafts, and wet updrafts using the proposed object identification method. We choose to keep the physical variables instead of non-dimensionalizing to preserve physical insights and due to an unclear choice of normalization variable. Other studies such as Schulz and Mellado (2018) or Salesky et al. (2017) only examine shear at the top or the bottom and then the normalization approach is dictated based on the respective scales. But in our study both top and surface conditions are varied.

3.1 Time evolution

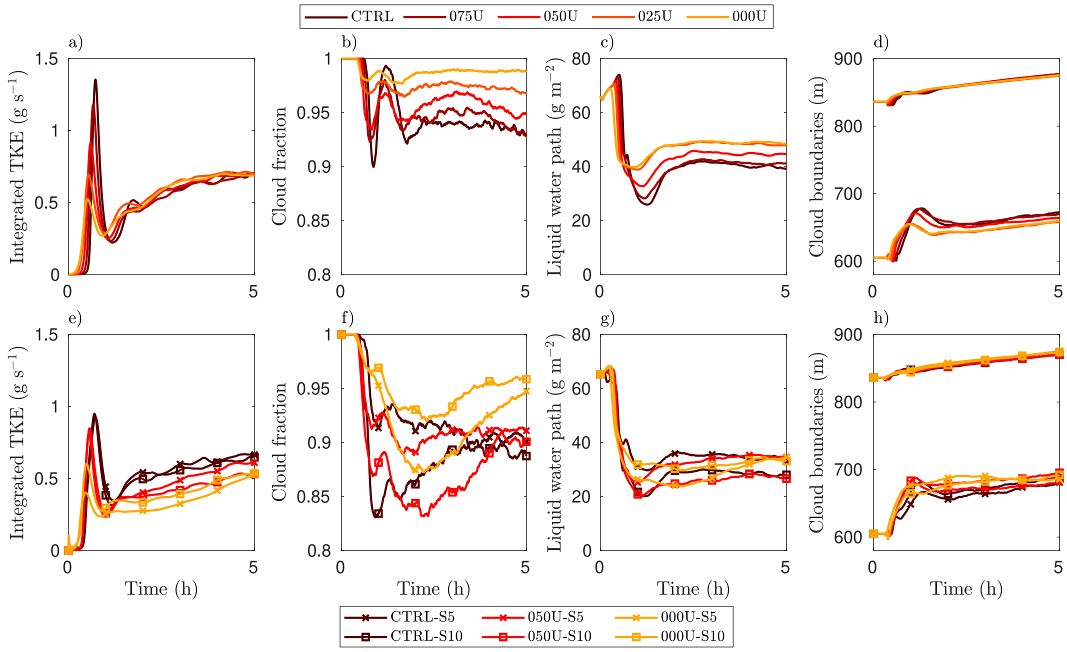

Figure 3. Time evolution of domain properties for all cases with a time resolution of 15 s, including (a,e) vertically integrated TKE, (b,f) cloud fraction, (c,g) LWP, and (d,h) mean cloud base and top heights.

For most cases, the evolution of vertically integrated TKE, cloud fraction and liquid water path (LWP) reaches a stable state around hour 3, after the spin-up period (Fig. 3). Only for the top sheared cases, cloud fraction still evolves at hour 3, stabilizing between hours 4 and 5. Therefore, we perform the rest of the analyses at either a snapshot at hour 4 (for the structure detection) or the 15 minutes ending at hour 4 (representing 1 eddy turnover time for turbulence statistics).

Shear has a strong effect on aggregated cloud properties. The surface shear cases all show a link between stronger surface shear and reduced cloud fraction, liquid water path (LWP), and cloud thickness (Fig. 3b-d,f-h). The top sheared cases show a similar tendency where the presence of top shear reduces cloud fraction and LWP for the 050U-S5,S10 and CTRL-S5,S10 cases. For the 000U-S5,S10 cases the results are inconsistent; LWP is similar and cloud fraction slightly increases for stronger top shear.

3.2 Thermodynamic profiles and turbulent fluxes

We observe slight differences in the average thermodynamic profiles that help to explain the differences in LWP, cloud thickness, and cloud fraction. The profiles of total water mixing ratio $q_t(z)$ and liquid water potential temperature $\theta_l(z)$ seem similar for all cases but closer inspection reveals different slopes within the STBL and different transitions in the inversion region. The 000U case has the most well-mixed profiles (Fig. 4a,c), the coldest STBL (lowest $\theta_l(z)$), and a sharp inversion (Fig. 4b,d). The well-mixedness

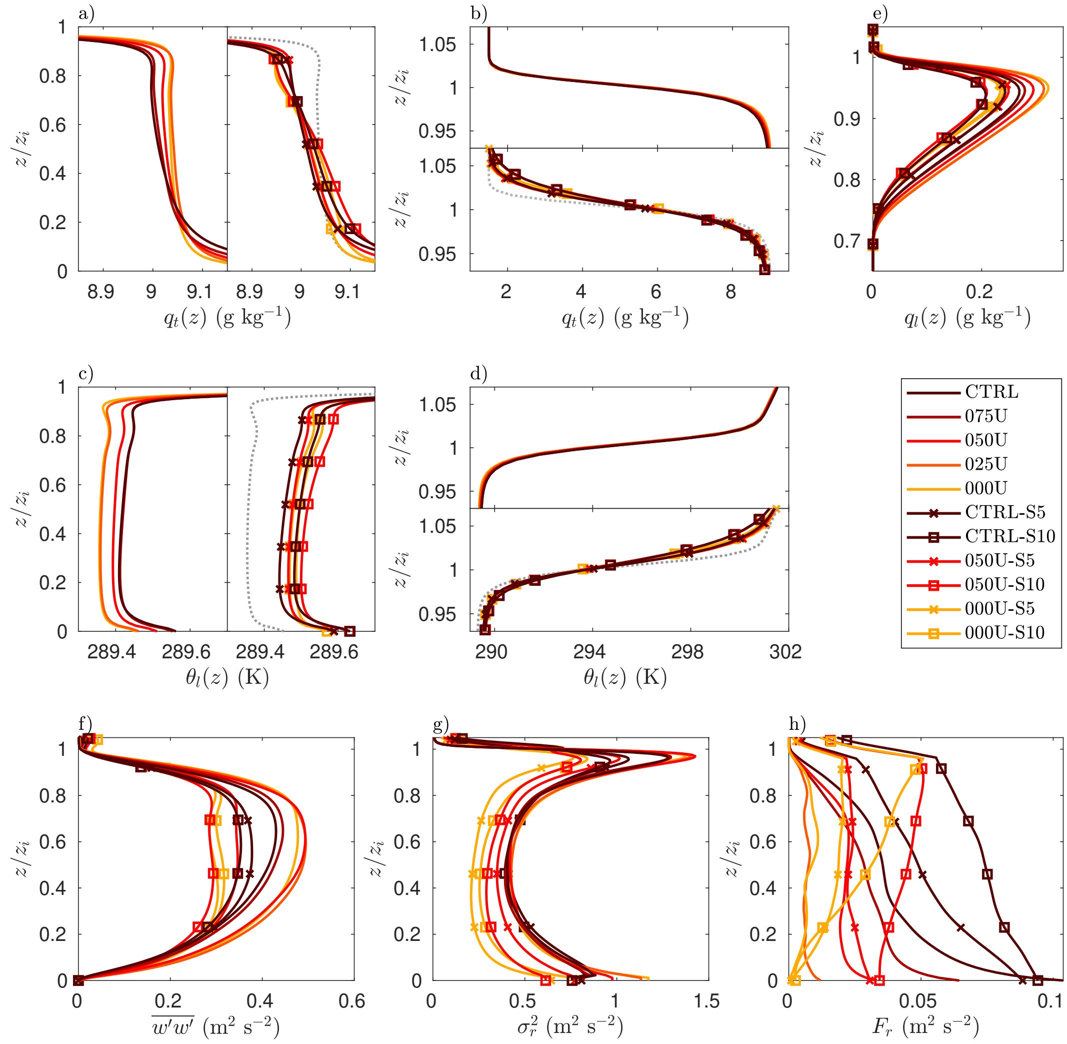

Figure 4. Vertical domain-averaged profiles of total water mixing ratio $q_t(z)$ with a closer look at (a) the boundary layer and (b) the inversion region; liquid water potential temperature $\theta_l(z)$ with a closer look at (c) the boundary layer and (d) the inversion region; and (g) liquid water mixing ratio $q_l(z)$. Turbulence statistics of (f) vertical velocity variance $\overline{w'w'}$, (g) net horizontal velocity variance σ_r^2, and (h) net horizontal momentum flux F_r. All profiles are 15 minute averages at hour 4. Gray dashed lines display the 000U for ease of comparison to top-sheared cases.

leads to a more adiabatic profile of liquid water mixing ratio $q_l(z)$ (Fig. 4e), explaining the greatest LWP in Fig. 3c.

All cases with only surface shear show a consistent sharp inversion region. Stronger surface sheared cases display a warmer STBL, which could be caused by the reduced cooling of a thinner cloud layer. The cases with top shear all display less well-mixed profiles than the surface-sheared cases. This is an interesting result, as it shows that the top shear indeed affects the rest of the STBL. The dilution of the inversion region (i.e. a less sharp inversion) for the top sheared cases has been extensively reported and linked to reduced cloud fraction due to increased mixing atop and entrainment into the STBL (McMichael et al., 2019; Kopec et al., 2016; Mellado et al., 2014; Wang et al., 2012, 2008).

The turbulent fluxes also show distinct features of surface and top shear. Stronger surface shear weakens $\overline{w'w'}$ but not the sum of horizontal velocity variances $\sigma_r^2 = \overline{u'u'}^2 + \overline{v'v'}^2$, resulting in a similar TKE profile (Fig. 4f,g). Stronger top shear reduces both $\overline{w'w'}$ and σ_r^2, and shows early signs of decoupling in the 000U-S5, 000U-S10, 050U-S5, and 050U-S10 cases, as evidenced by the reduced vertical velocity variance in the center of the STBL surrounded by two local maxima. The sum of horizontal momentum fluxes $F_r = (\overline{u'w'}^2 + \overline{v'w'}^2)^{1/2}$ as computed by Lin et al. (1996) exhibits signatures of both surface and top shear, in that – considering the gradient of F_r – an increased downward momentum transport develops for the 000U-S5, 000U-S10, and 050U-S10 cases. The buoyancy and heat fluxes (not shown) are consistent with the differences in cloud thickness and LWP, with stronger surface and top shear developing weaker in-cloud and subcloud buoyancy fluxes.

Finally, while the enhanced turbulent mixing for increased top shear is evident in the thickening of the inversion region, we also compute the entrainment velocity as

$$w_e = \frac{dz_i}{dt} + Dz_i \tag{4}$$

where the large scale divergence $D = 3.75 \times 10^{-6}$ s^{-1} (Stevens et al., 2005). Table 1 shows that the average entrainment rate is nearly identical for the cases without top shear, in agreement with Fedorovich and Conzemius (2008), who argued that entrainment for larger bottom shear was artificially enhanced by the development of top shear, which we deliberately avoided by nudging the velocity in the whole domain. Top shear does not show a clear effect on w_e: CTRL-S10 and 000U-S10 entrain stronger but CTRL-S5 and 050U-S5,S10 entrain weaker than the cases without top shear. Since the entrainment rate is sensitive to the definition of z_i (Schulz & Mellado, 2018) (here: where the gradient of θ_l is maximum), as well as to the cloud content in each case due to the cloud-radiation feedback (Matheou & Teixeira, 2019), and since we cannot isolate this feedback, we cannot confirm the expected increased entrainment velocity with stronger top shear (Schulz & Mellado, 2018; Wang et al., 2012).

According to Schulz and Mellado (2018), who used the same base case in a DNS study on top shear, a critical $\Delta r \simeq 4w_{*,\mathrm{cld}}$ marks the transition from convection-dominated to shear-dominated flow in the top stratification layer. This criterion places all of our S5 and S10 cases in the shear-dominated regime (Table 1), where buoyancy reversal could occur and destabilize the cloud layer. Implications of the dominant physics regime for the spatial arrangement of coherent structures are not obvious. Schulz and Mellado (2018) also derived that a velocity jump of 10 m s^{-1} would achieve "critical depletion", i.e. a level of thinning that reduces the radiative cooling flux by 5%. In our simulations, all the top-sheared cases reduce the LWP and weaken the radiative flux more than 5% when compared to the 000U case (see Table 1, where we report the difference of $\Delta F_{\mathrm{rad}} = F_{\mathrm{rad}}(z_i) - F_{\mathrm{rad}}(z_b)$, the net longwave radiative flux divergence between the STBL top and mean cloud base). A possible cause of depletion occurring below the proposed threshold of 10 m s^{-1} is that Schulz and Mellado (2018) assumed an adiabatic profile for $q_l(z)$ for the derivation of the threshold, while in fact our simulations show that top shear causes the $q_l(z)$ profile to be sub-adiabatic (Fig. 4e).

3.3 Spatial organization of the STBL

A first glimpse at the behavior of LWP and vertical velocity in the domain shows a distinct spatial structure and features when varying surface and top wind shear (Figs. 5 and 6). In the 000U case without surface and top shear, updrafts develop as plumes, displaying a network-like cellular organization in the regions where they form and a solid cohesive form in the regions where they fully develop and terminate. In contrast, in the strongly sheared CTRL case, subcloud roll structures appear (white aligned areas). We will see that this behavior is captured in the updraft and downdraft object identification in the next Section. In a CBL, the transition between cells and rolls occurs for $\eta \simeq$

Table 1. Resulting parameters for the different cases averaged from 3:45-4:00 h

	Units	CTRL	075U	050U	025U	000U	CTRL -S5	CTRL -S10	050U -S5	050U -S10	000U -S5	000U -S10
z_i	m	870	871	870	868	869	867	864	868	864	868	868
z_b	m	666	665	658	651	653	672	680	675	686	686	685
h	m	205	206	212	217	216	196	184	193	177	183	182
w_e	mm/s	4.82	4.99	4.87	4.86	4.83	4.19	5.11	4.36	4.42	4.95	5.24
w_*	m/s	0.84	0.83	0.82	0.81	0.81	0.84	0.84	0.82	0.82	0.81	0.81
$w_{*,\mathrm{cld}}$	m/s	0.57	0.59	0.62	0.63	0.64	0.52	0.50	0.54	0.49	0.55	0.55
u_*	m/s	0.32	0.25	0.18	0.11	0.01	0.30	0.31	0.17	0.19	0.03	0.05
$u_{*,\mathrm{top}}$	m/s	0.07	0.05	0.05	0.04	0.04	0.16	0.24	0.15	0.22	0.14	0.22
Δr	m/s	0.10	0.06	0.02	0.002	0.02	5.7	10.4	5.0	9.7	4.8	9.3
$\Delta r/w_{*,\mathrm{cld}}$	-	0.18	0.09	0.03	0.004	0.03	10.9	20.8	9.4	19.9	8.7	16.9
L_{ob}	m	-121	-61.7	-24.1	-5.45	-0.001	-95.8	-105	-21.2	-24.8	-0.11	-0.53
η	-	7.18	14.1	36	159	653,850	9.05	8.25	40.9	34.7	7,679	1,630
$\frac{\Delta F_{\mathrm{rad}}}{\Delta F_{\mathrm{rad,\ 000U}}}$	%	90.2	92.3	95.1	97.0	100	86.1	83.8	88.1	82.0	87.7	91.0

15−20 (Salesky et al., 2017), which is in agreement with our simulations: only the CTRL ($\eta = 7.2$) and 075U ($\eta = 14.1$) cases show evidence of rolls (Fig. 5 and Table 1). The flow near the top does not develop streaky structures when the top shear is strong, since the stratified shear layer acts differently than a wall. The cellular shape near the top shows weaker negative velocities when the top shear is strong and some alignment in the direction of the wind shear. This is also reflected in the shape of the clouds when looking at LWP (top row), with a regular cellular pattern in most cases and cloud elements aligning in the direction of the wind only for the CTRL-S10 case. This suggests that both strong surface and top shear are necessary to influence the shape of the cloud field. Downdraft regions display a network-like structure near the top of the ABL, but upon entering the subcloud region downdraft regions transition into occupying the free spaces left by the updrafts.

Fig. 7 shows the cloud top height z_t field (the last height at which we encounter liquid water), where the strongly top-sheared cases (bottom row) present signs of gravity waves. The observed wavelength is of the order of 1 km, which matches the Kelvin-Helmholtz instability theory for combined buoyancy and shear (Drazin, 2002): the theoretical critical wavelength is $\lambda = \frac{\pi\theta_{v0}\Delta r^2}{g\Delta\theta_v}$, where Δr and $\Delta\theta_v$ are the initial values of the wind speed magnitude and virtual potential temperature jump across the inversion region. For strong top shear (the S10 cases), $\lambda = 1.28$ km (yellow pattern in Fig. 7), agrees with the pattern seen at z_t. Meanwhile, for weaker top shear (S5 cases), the expected $\lambda = 312$ m is not observed in z_t for our simulations. The chosen LES grid spacing should be able to capture the gravity waves, although not with great resolution; $\Delta x =$ 35 m places 6 points within a wave period of 300 m oriented at a 45^o angle, while the observed shear layer of thickness O(30 m) would also be resolved by 6 points in the vertical. There could also be a critical length scale for waves to affect the cloud top; more top-shear cases would need to be analyzed to confirm this hypothesis. Nevertheless, gravity waves shaping the cloud top enhance the variability of LWP.

3.4 Updraft and downdraft objects

3.4.1 Spatial distribution and geometric properties

Fig. 8 shows a three-dimensional visualization of the objects identified as large (categories I and II) for the cases CTRL, 000U, CTRL-S10, and 000U-S10, with detailed views of portions of updraft and downdraft objects for each case. A clear feature of surface shear

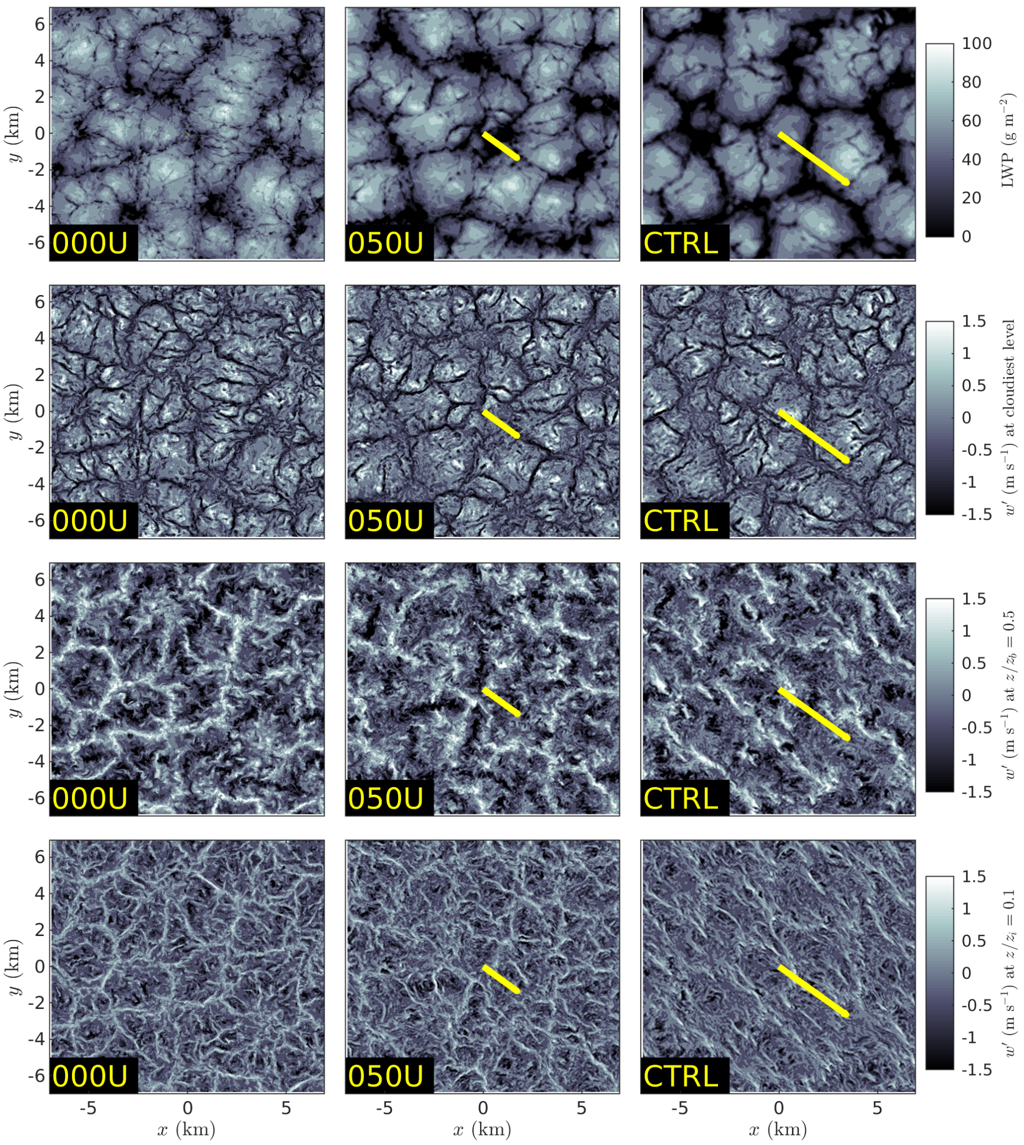

Figure 5. Spatial snapshots at hour 4 for the cases with no top shear. LWP (top) and vertical velocity near the surface ($z = 0.1z_i$, bottom), in the subcloud region ($z = 0.5z_b$, middle bottom), and in the cloud region (at the height of maximum cloud fraction, middle top). Yellow lines show the velocity vector.

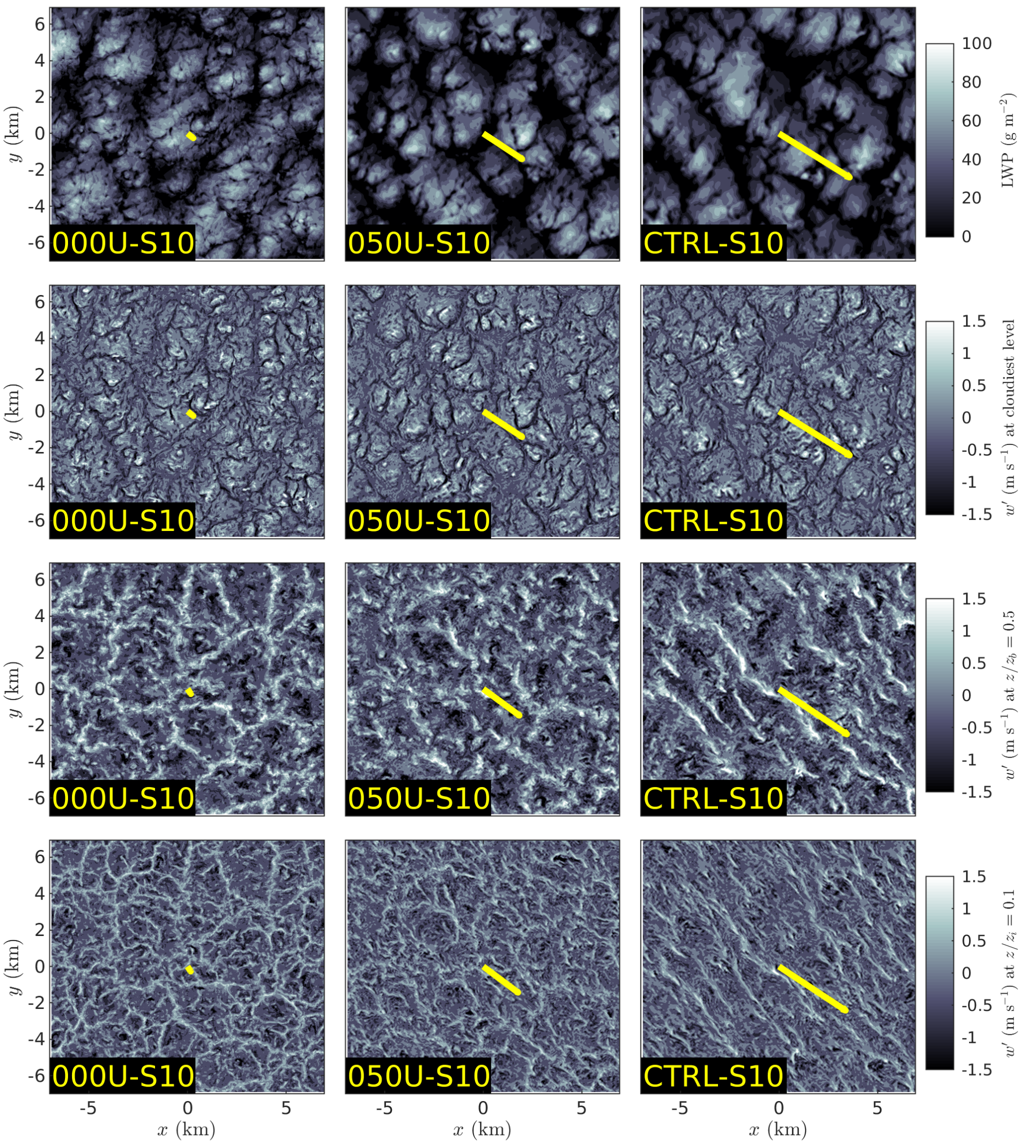

Figure 6. Spatial snapshots at hour 4 for strongly top sheared cases. LWP (top) and vertical velocity near the surface ($z = 0.1z_i$, bottom), in the subcloud region ($z = 0.5z_b$, middle bottom), and in the cloud region (at the height of maximum cloud fraction, middle top). Yellow lines show the velocity vector.

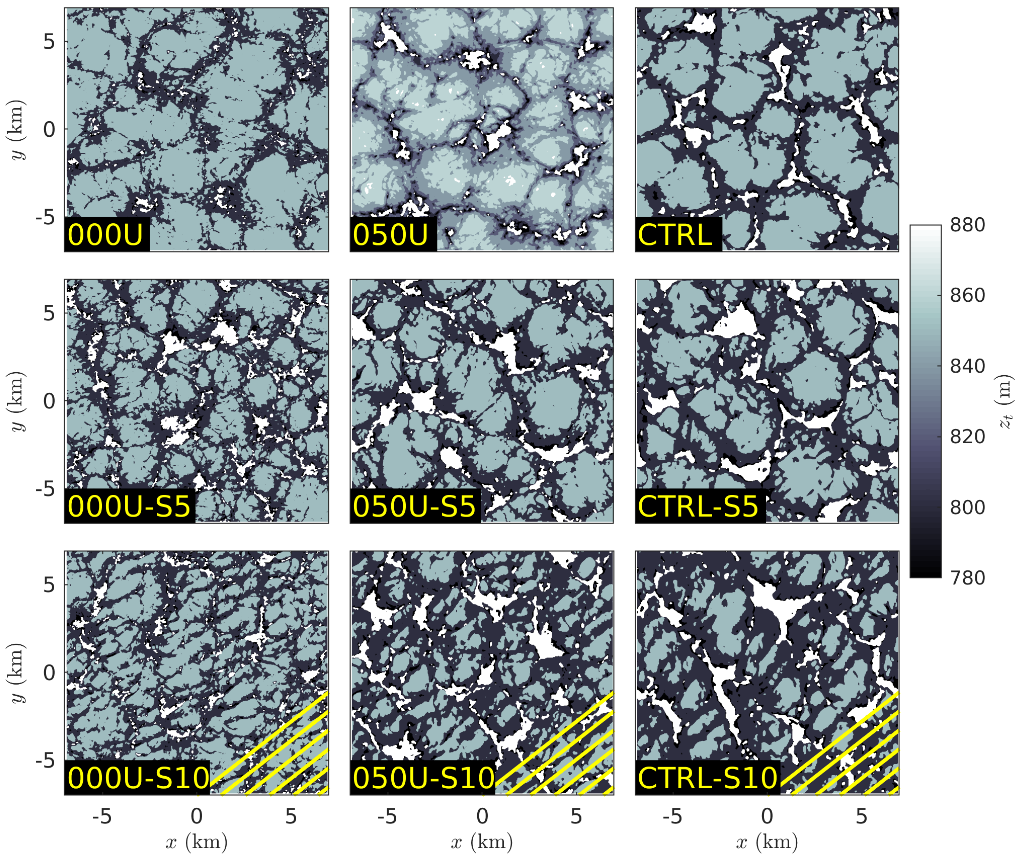

Figure 7. Spatial snapshot of cloud top heights (last height with liquid water content) for different cases at hour 4. Yellow lines mark the theoretical wavelength pattern expected for the strongly sheared cases. Colormap limits do not cover the full range of observed values to enhance the visual contrast.

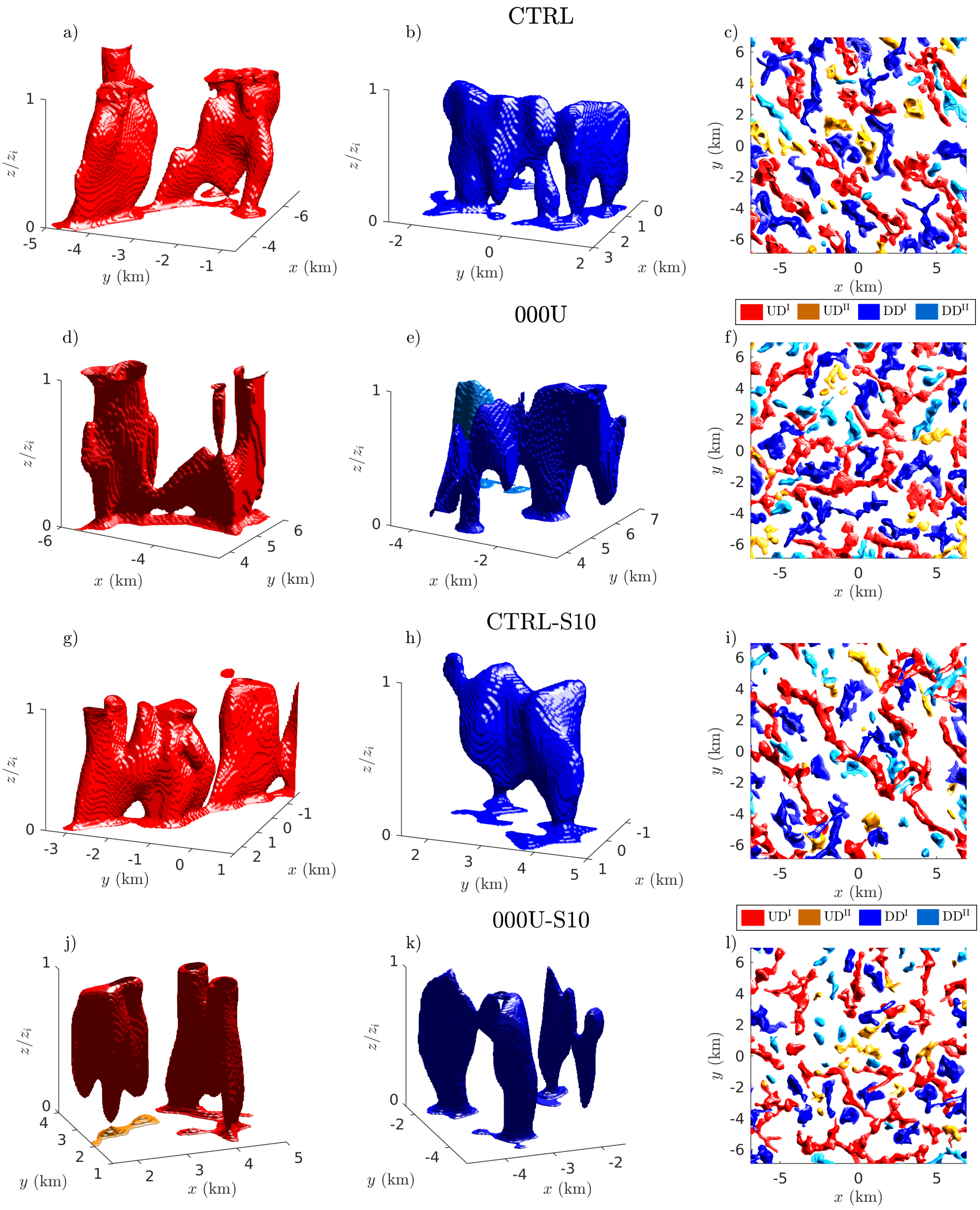

Figure 8. Three-dimensional visualization of identified large updraft and downdraft objects in the CTRL (top row), 000U (second row), CTRL-S10 (third row), and 000U-S10 (bottom row) cases: a,d,g,j) show portions of the domain including a large updraft object, b,e,h,k) a large downdraft object, and c,f,i,l) show a top view of the large udpraft and downdraft objects identified in the full domain.

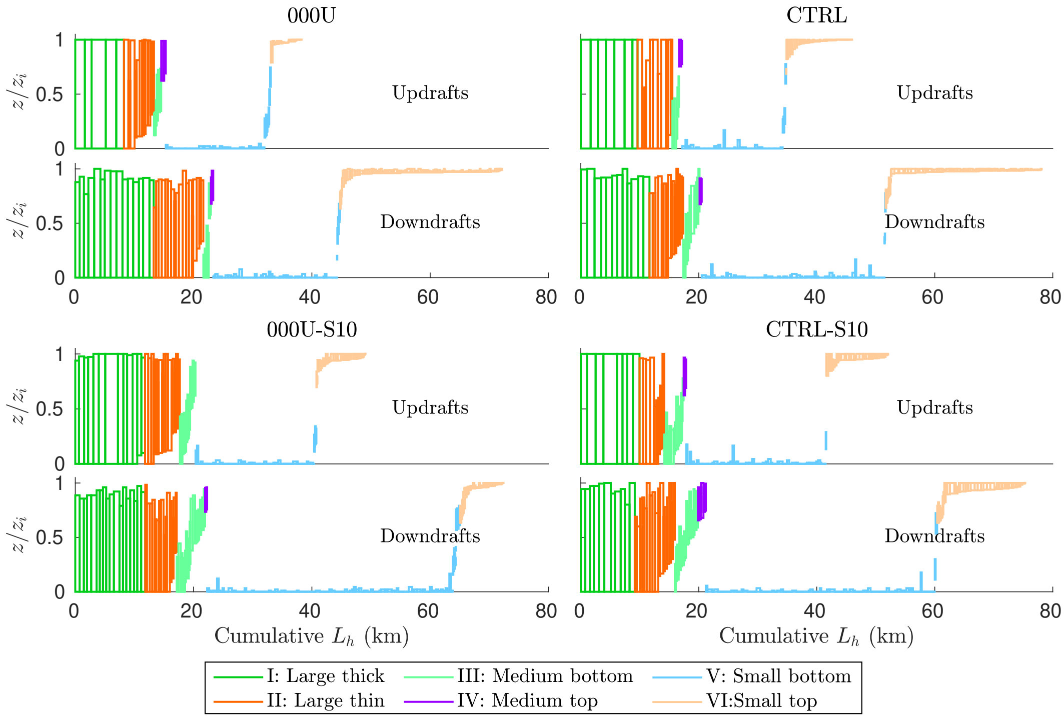

Figure 9. Distribution of updrafts and downdraft objects by case. The different object categories are labeled by color, and their distribution in space is described by their vertical position and cumulative horizontal length L_h. Objects I and II correspond to large objects spanning the whole STBL separated into thicker and thinner objects, III and IV are medium objects separated by their origin into bottom and top objects, and V and VI are small objects also separated into bottom and top objects.

is the change in vertical inclination of the updraft objects but the downdraft objects are not inclined. Meanwhile, top shear modifies the top region of updraft objects, with a more rounded shape likely to be caused by the enhanced mixing at the top. Updrafts objects can split into several vertical branches in the upper part of the STBL that are typically connected in the surface and subcloud regions while downdrafts tend to be connected near cloud top. The network structure mentioned in the previous section is not observed in the large objects. Large updraft objects organize in the direction of the wind for the CTRL case, which gives rise to the overall roll structure in the STBL.

Fig. 9 shows the distribution of the different objects within the STBL by their assigned category. The general distribution of the objects is similar for all cases. A key difference is the development of more medium sized updraft objects (III and IV) with stronger surface shear, as well as the reduction of top small objects (VI) for downdrafts with stronger top shear, similarly to the change in the top of the updraft objects (Fig. 8g,j), likely due to enhanced mixing. Large updraft objects (I and II) tend to always reach the top of the STBL, and the thickest large objects (I) are connected to the surface in all cases, while some thinner large objects (II) terminate or start around z/z_i of 0.1 to 0.3. Similarly, large downdraft objects (I and II) tend to reach the surface, but originate at varying heights near the STBL top, mostly around $z/z_i = 0.9$. Even though we observed early signs of decoupling in Fig. 4, there is no manifestation of decoupling in the updraft and downdraft objects.

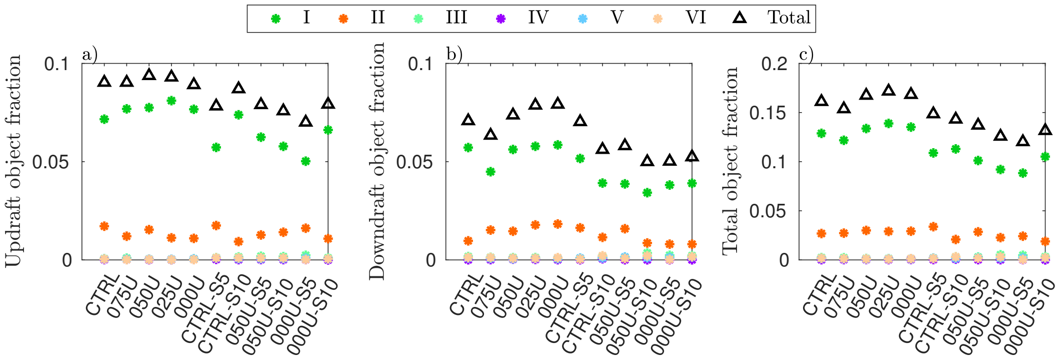

Figure 10. Volume fractions per object type in the STBL for (a) updrafts, (b) downdrafts, and (c) total of updrafts and downdrafts.

The actual volume occupied by updrafts and downdrafts combined does not surpass 20% of the total STBL (Fig. 10c), with only the large objects (I and II) having a significant volume fraction. Updrafts always occupy more space than downdrafts, and both updraft and downdraft volume fractions decrease with top shear. We find that the total volume fraction of updrafts and downdrafts is strongly correlated to both LWP and the maximum vertical velocity variance in the profile, with correlation coefficients of 89.4% and 96.4%, respectively.

3.4.2 Contribution to turbulent fluxes

Updrafts and downdrafts contribute significantly to turbulent fluxes. We compute the contributions by conditionally sampling the covariance contained in each of the different categories of objects (I to VI), finding that the large objects (I and II) contribute the most, as expected because of their larger volume fraction. Fig. 11h-l shows the mean ratios $R_{w'w'}$, $R_{w'\theta_v'}$, $R_{w'q_t'}$, $R_{w'\theta_l'}$, and R_{F_r}, computed as vertical averages of the portion of total turbulent fluxes explained by the large objects (I and II), for all cases. On average, 33% of the total vertical velocity variance $\overline{w'w'}$, 53% of the total buoyancy flux, and 52% of the net momentum flux are contained in the large objects (I and II). The contribution of large downdrafts (I and II) to $\overline{w'w'}$ weakens with stronger top-shear (Fig. 11h), which can be explained by the reduced cloud fraction and radiative cooling caused by the enhanced top mixing. This is demonstrated when comparing the CTRL, CTRL-S5 and CTRL-S10 cases: while the updraft contribution remains identical, the downdraft portion decreases with stronger top shear, causing an overall reduction of $\overline{w'w'}$. The mean vertical velocity of the UD^{I} and DD_{I} objects also decreases with top-shear (not shown), with downdraft velocities weakening more than updrafts. For the total $\overline{w'q_t'}$ the large objects (I and II) account for 42% of the fluxes, on average, and for $\overline{w'\theta_l'}$, large objects account for 53%.

Some of these ratios can be misleading, as (i) they are vertical averages; (ii) the $\overline{w'\theta_l}$ and $\overline{w'\theta_v}$ profiles change sign; (iii) ratios of small values are not accurate and have been omitted in the vertical averaging; and (iv) the $\overline{w'q_t'}$ profile does not change sign but can have positive or negative contributions. Instead the complete picture of the contributions should be used for interpretation (see Figure S3 for detailed profiles). The challenges in computing the large object contributions may explain why we obtain different values than Brient et al. (2019), who reported 75% for moisture and 79% for heat fluxes. Other reasons include the use of a different base case, and intrinsic differences in their tracer methodology and parameter selection. While there are known differences in the detection of updraft and downdraft regions between tracer and field variable methods

(Couvreux et al., 2010), these differences are expected to be greater in the surface and top regions. Even in the middle of the STBL, the updraft and downdraft contribution is smaller in our case.

A summary of the effect of wind shear conditions on different properties of the STBL is shown in Fig. 11. First, cloud fraction and LWP are sensitive to both surface and top wind shear (Fig. 11a,b), with a general trend of less clouds with increased surface and top wind shear. As discussed previously, the trend of entrainment rate is not clear in the cases studied (Fig. 11c) even though there is evidence of increased mixing in the growth of the shear layer. We also saw a decrease in vertical velocity variance with surface and top shear (Fig. 11d), where interestingly the maximum velocity variance $\overline{w'w'}_{\max}$ is strongly correlated to LWP (correlation coefficient of 95%). Well-mixedness was also strongly affected by shear; Fig. 11e,f shows the mean slope of q_t and θ_l calculated between $0.2z_i$ and $0.8z_i$, with well-mixed conditions prevailing for weaker surface and weaker top shear. Another interesting finding is that the total volume fraction of all the updraft and downdraft objects is sensitive to shear conditions; moreover, this dependence strongly correlates to $\overline{w'w'}_{\max}$ due to their definition depending on vertical velocity (corr. coef. of 97%). Lastly, the contributions of the large (I and II) updraft and downdraft objects to the total turbulent fluxes in the STBL are also affected by both surface and top wind shear in different ways, with only the mean ratio $R_{w'q'_t}$ seeming independent of top wind shear (Fig. 11h-l).

3.5 Wet updrafts

Lastly, we analyze the position of the identified wet updrafts as shown in Fig. 12. For the weakly top-sheared cases, the cloud centers are more uniformly distributed in height and size than in the strongly top-sheared cases. One possible cause is that the enhanced mixing caused by top shear inhibits the development of smaller cloud centers near the top of the STBL, similarly to updrafts changing their upper shape with top shear (Fig. 8a,d,g,j).

Fig. 13 confirms that the identified wet updrafts are collocated with updrafts: between 50% and 60% of the cloud centers volume is contained in updraft objects, while nearly none is contained in downdraft objects. This is not obvious as the definition of cloud center objects is solely based on LWP and does not contain any condition for vertical velocity.

4 Conclusions

We analyzed the effect of surface and top wind shear on the spatial organization of a Stratocumulus-topped boundary layer. We used LES simulations of the DYCOMS II RF01 base case with wind profile variations. We also performed a spatial identification of coherent updrafts, downdrafts, and wet updraft objects, classified them by location and size distribution, and described how they are affected by shear.

Surface shear affects the spatial organization of the clouds as well as the vertical profiles that characterize the STBL. Weak surface shear organizes the updrafts in plume-like structures while strong surface shear creates rolls. The former causes strongly well-mixed thermodynamic profiles that result in an increased cloud fraction and LWP. Rolls are observed for values of $-z_i/L_{ob} < 15$, in agreement with the transition for CBLs (Salesky et al., 2017). The effect of weaker surface shear is opposite to the reduced cloud fraction for shallow cumulus clouds (Park et al., 2017).

Stronger top shear also decreases cloud fraction and LWP by thinning the cloud from the top, as expected from previous studies (Wang et al., 2012; Schulz & Mellado, 2018). Cloud thinning also weakens the downdraft contribution to the turbulent fluxes,

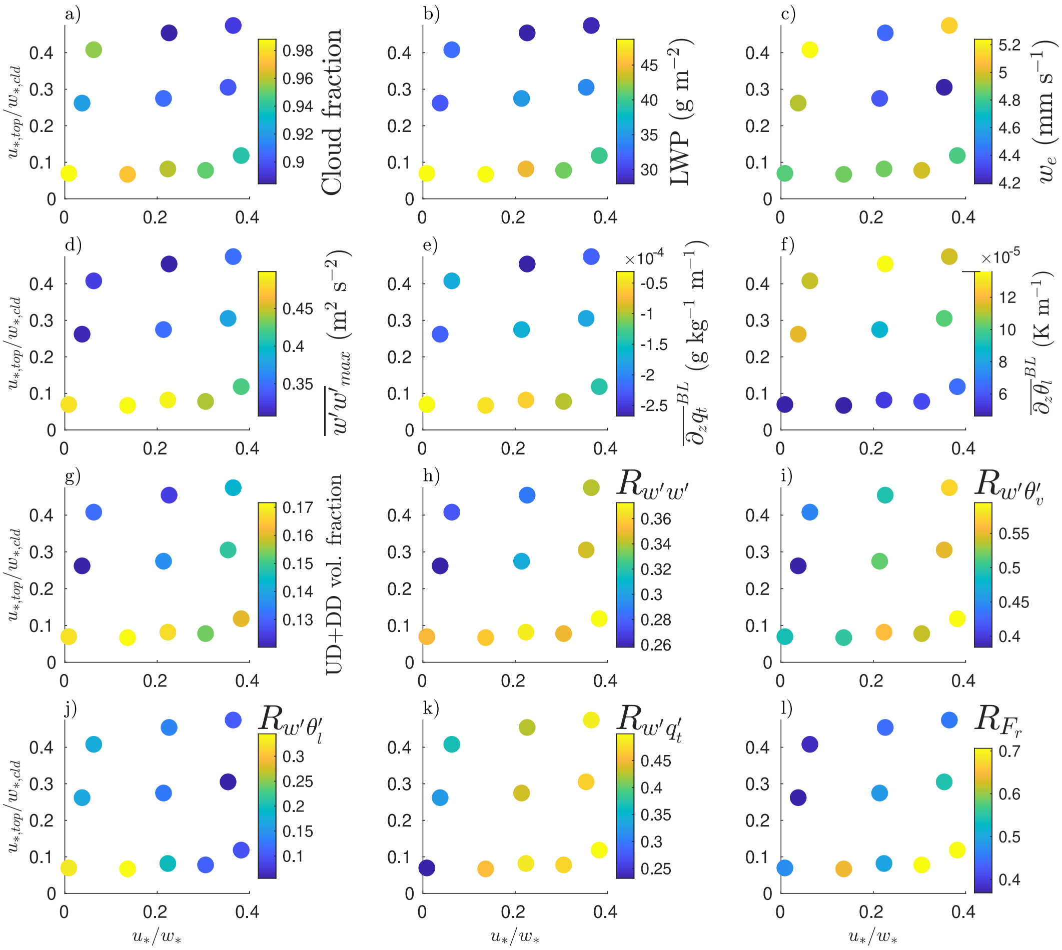

Figure 11. Summarized results at hour 4, presented in the parameter space of surface wind shear u_*/w_* and top wind shear $u_{*,top}/w_{*,cld}$ for (a) cloud fraction, (b) LWP, (c) entrainment rate w_e, (d) maximum velocity variance $\overline{w'w'}_{\max}$, (e) the mean slope of q_t between $0.2z_i$ and $0.8z_i$, $\overline{\partial_z q_t}^{\mathrm{BL}}$, (f) the mean slope of θ_l between $0.2z_i$ and $0.8z_i$, $\overline{\partial_z \theta_l}^{\mathrm{BL}}$, (g) updraft object volume fraction in the STBL; mean contributions of large objects to the (h) vertical velocity variance $R_{w'w'}$, (i) buoyancy flux $R_{w'\theta_v'}$, (j) heat flux $R_{w'\theta_l'}$, (k) moisture flux $R_{w'q_t'}$, and (l) net horizontal momentum flux R_{F_r}.

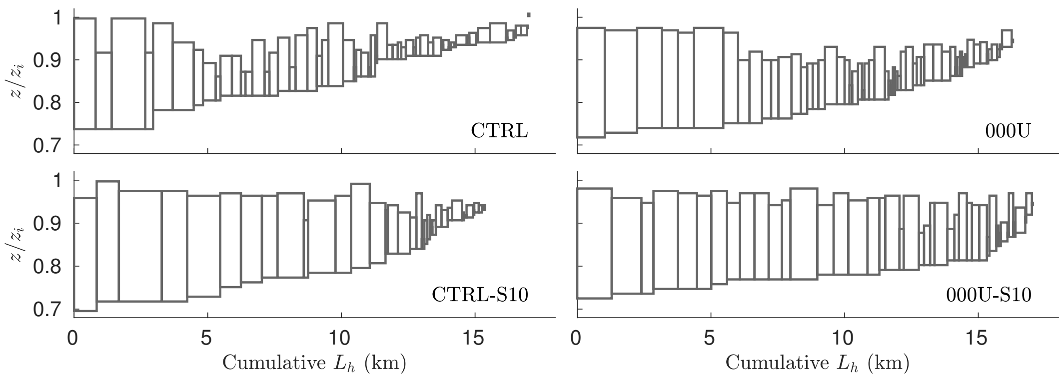

Figure 12. Distribution of wet updraft object properties by case. The wet updraft properties are described by their vertical span and cumulative horizontal length L_h. Objects are ordered by their base height.

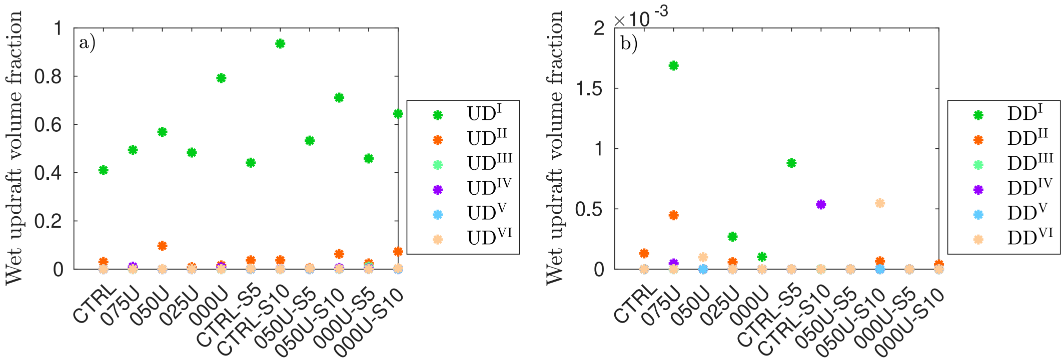

Figure 13. Volume fraction of cloud centers contained in each of the different classes of a) updrafts and b) downdrafts.

with indications of early decoupling observed for the cases with stronger top than surface shear. Gravity waves were also observed for strong top shear, shaping the top of the cloud layer and flow near the inversion region. Combined strong surface and top wind shear caused the clouds to be elongated in the direction of the mean wind.

Classifying the updraft and downdraft objects by size and position shows that objects that span the whole STBL dominate in terms of volume and are responsible for a large portion of the turbulent fluxes, explaining –on average for all cases– 33% of the total vertical velocity variance and 53% of the total buoyancy flux. This confirms a classic assumption used in the development of turbulence parameterizations. When surface shear is strong, updrafts tilt in the direction of the wind, and updrafts and downdrafts connect in the mean wind direction. When top shear is strong, the enhanced mixing changes the shape of the top of updrafts and inhibits the presence of wet updrafts near the top of the STBL.

Future work should examine other definitions of updrafts and downdrafts, other realistic conditions that can affect the organization of coherent structures in the STBL, as well as understanding the dynamics of these coherent structures during the course of the day or along Lagrangian trajectories.

Acknowledgments

We thank Elynn Wu and José Ortíz Tarín for helpful discussion and comments. MZZ was funded by CONICYT PFCHA/DOCTORADO BECAS CHILE/2015 - 72160605. TH was supported by the U.S. Department of Energy's Atmospheric System Research, an Office of Science, Office of Biological and Environmental Research program, under Grant DE-SC0017999. The code used for the analysis is available at `https://doi.org/10.5281/zenodo.4116253`. The authors declare no conflict of interest.

References

Atkinson, B. W., & Zhang, J. W. (1996). Mesoscale shallow convection in the atmosphere. *Reviews of Geophysics*, *34*(4), 403–431. doi: 10.1029/96RG02623

Brient, F., Couvreux, F., Villefranque, N., Rio, C., & Honnert, R. (2019). Object-Oriented Identification of Coherent Structures in Large Eddy Simulations: Importance of Downdrafts in Stratocumulus. *Geophysical Research Letters*, *46*(5), 2854–2864. doi: 10.1029/2018GL081499

Chinita, M. J., Matheou, G., & Teixeira, J. (2018). A Joint Probability Density–Based Decomposition of Turbulence in the Atmospheric Boundary Layer.

Monthly Weather Review, *146*(2), 503–523. doi: 10.1175/MWR-D-17-0166.1
Clemesha, R. E. S., Gershunov, A., Iacobellis, S. F., & Cayan, D. R. (2017). Daily variability of California coastal low cloudiness: A balancing act between stability and subsidence. *Geophysical Research Letters*, *44*(7), 3330–3338. doi: 10.1002/2017GL073075
Couvreux, F., Hourdin, F., & Rio, C. (2010). Resolved Versus Parametrized Boundary-Layer Plumes. Part I: A Parametrization-Oriented Conditional Sampling in Large-Eddy Simulations. *Boundary-Layer Meteorology*, *134*(3), 441–458. doi: 10.1007/s10546-009-9456-5
Davini, P., D'Andrea, F., Park, S.-B., & Gentine, P. (2017). Coherent Structures in Large-Eddy Simulations of a Nonprecipitating Stratocumulus-Topped Boundary Layer. *Journal of the Atmospheric Sciences*, *74*(12), 4117–4137. doi: 10.1175/JAS-D-17-0050.1
Drazin, P. G. (2002). *Introduction to hydrodynamic stability.* Cambridge University Press. doi: 10.1017/CBO9780511809064
Fedorovich, E., & Conzemius, R. (2008). Effects of wind shear on the atmospheric convective boundary layer structure and evolution. *Acta Geophysica*, *56*(1), 114–141. doi: 10.2478/s11600-007-0040-4
Ghonima, M. S., Heus, T., Norris, J. R., & Kleissl, J. (2016). Factors Controlling Stratocumulus Cloud Lifetime over Coastal Land. *Journal of the Atmospheric Sciences*, *73*(8), 2961–2983. doi: 10.1175/JAS-D-15-0228.1
Han, J., & Bretherton, C. S. (2019). TKE-Based Moist Eddy-Diffusivity Mass-Flux (EDMF) Parameterization for Vertical Turbulent Mixing. *Weather and Forecasting*, *34*(4), 869–886. doi: 10.1175/WAF-D-18-0146.1
Kim, S.-W., Park, S.-U., & Moeng, C.-H. (2003). Entrainment Processes in the Convective Boundary Layer with Varying Wind Shear. *Boundary-Layer Meteorology*, *108*(2), 221–245. doi: 10.1023/A:1024170229293
Kopec, M. K., Malinowski, S. P., & Piotrowski, Z. P. (2016). Effects of wind shear and radiative cooling on the stratocumulus-topped boundary layer. *Quarterly Journal of the Royal Meteorological Society*, *142*(701), 3222–3233. doi: 10.1002/qj.2903
Lilly, D. K. (1968). Models of cloud-topped mixed layers under a strong inversion. *Quarterly Journal of the Royal Meteorological Society*, *94*(401), 292–309. doi: 10.1002/qj.49709440106
Lin, C., McWilliams, J. C., Moeng, C., & Sullivan, P. P. (1996). Coherent structures and dynamics in a neutrally stratified planetary boundary layer flow. *Physics of Fluids*, *8*(10), 2626–2639. doi: 10.1063/1.869048
Matheou, G., & Teixeira, J. (2019). Sensitivity to Physical and Numerical Aspects of Large-Eddy Simulation of Stratocumulus. *Monthly Weather Review*, *147*(7), 2621–2639. doi: 10.1175/MWR-D-18-0294.1
McMichael, L. A., Mechem, D. B., Wang, S., Wang, Q., Kogan, Y. L., & Teixeira, J. (2019). Assessing the mechanisms governing the daytime evolution of marine stratocumulus using large-eddy simulation. *Quarterly Journal of the Royal Meteorological Society*, *145*(719), 845–866. doi: 10.1002/qj.3469
Mellado, J. P., Stevens, B., & Schmidt, H. (2014). Wind Shear and Buoyancy Reversal at the Top of Stratocumulus. *Journal of the Atmospheric Sciences*, *71*(3), 1040–1057. doi: 10.1175/JAS-D-13-0189.1
Moeng, C.-H., & Sullivan, P. P. (1994). A Comparison of Shear- and Buoyancy-Driven Planetary Boundary Layer Flows. *Journal of the Atmospheric Sciences*, *51*(7), 999–1022. doi: 10.1175/1520-0469(1994)051⟨0999:ACOSAB⟩2.0.CO;2
Park, S.-B., Böing, S., & Gentine, P. (2017). Role of Surface Friction on Shallow Nonprecipitating Convection. *Journal of the Atmospheric Sciences*, *75*(1), 163–178. doi: 10.1175/JAS-D-17-0106.1
Park, S.-B., Gentine, P., Schneider, K., & Farge, M. (2016). Coherent Structures in the Boundary and Cloud Layers: Role of Updrafts, Subsiding Shells, and Envi-

ronmental Subsidence. *Journal of the Atmospheric Sciences*, *73*(4), 1789–1814. doi: 10.1175/JAS-D-15-0240.1

Pedersen, J. G., Malinowski, S. P., & Grabowski, W. W. (2016). Resolution and domain-size sensitivity in implicit large-eddy simulation of the stratocumulus-topped boundary layer. *Journal of Advances in Modeling Earth Systems*, *8*(2), 885–903. doi: 10.1002/2015MS000572

Salesky, S. T., Chamecki, M., & Bou-Zeid, E. (2017). On the Nature of the Transition Between Roll and Cellular Organization in the Convective Boundary Layer. *Boundary-Layer Meteorology*, *163*(1), 41–68. doi: 10.1007/s10546-016-0220-3

Schulz, B., & Mellado, J. P. (2018). Wind Shear Effects on Radiatively and Evaporatively Driven Stratocumulus Tops. *Journal of the Atmospheric Sciences*, *75*(9), 3245–3263. doi: 10.1175/JAS-D-18-0027.1

Stevens, B., Moeng, C.-H., Ackerman, A. S., Bretherton, C. S., Chlond, A., de Roode, S., … Zhu, P. (2005). Evaluation of Large-Eddy Simulations via Observations of Nocturnal Marine Stratocumulus. *Monthly Weather Review*, *133*(6), 1443–1462. doi: 10.1175/MWR2930.1

Wang, S., Golaz, J.-C., & Wang, Q. (2008). Effect of intense wind shear across the inversion on stratocumulus clouds. *Geophysical Research Letters*, *35*(15). doi: 10.1029/2008GL033865

Wang, S., Zheng, X., & Jiang, Q. (2012). Strongly sheared stratocumulus convection: an observationally based large-eddy simulation study. *Atmospheric Chemistry and Physics*, *12*(11), 5223–5235. doi: 10.5194/acp-12-5223-2012

Wood, R. (2012). Stratocumulus Clouds. *Monthly Weather Review*, *140*(8), 2373–2423. doi: 10.1175/MWR-D-11-00121.1

Wu, E., Yang, H., Kleissl, J., Suselj, K., Kurowski, M. J., & Teixeira, J. (2020). On the Parameterization of Convective Downdrafts for Marine Stratocumulus Clouds. *Monthly Weather Review*, *148*(5), 1931–1950. doi: 10.1175/MWR-D-19-0292.1

Zelinka, M. D., Randall, D. A., Webb, M. J., & Klein, S. A. (2017). Clearing clouds of uncertainty. *Nature Climate Change*, *7*, 674–678. doi: 10.1038/nclimate3402

Zhou, X., & Bretherton, C. S. (2019). Simulation of Mesoscale Cellular Convection in Marine Stratocumulus: 2. Nondrizzling Conditions. *Journal of Advances in Modeling Earth Systems*, *11*(1), 3–18. doi: 10.1029/2018MS001448

Figure 1.

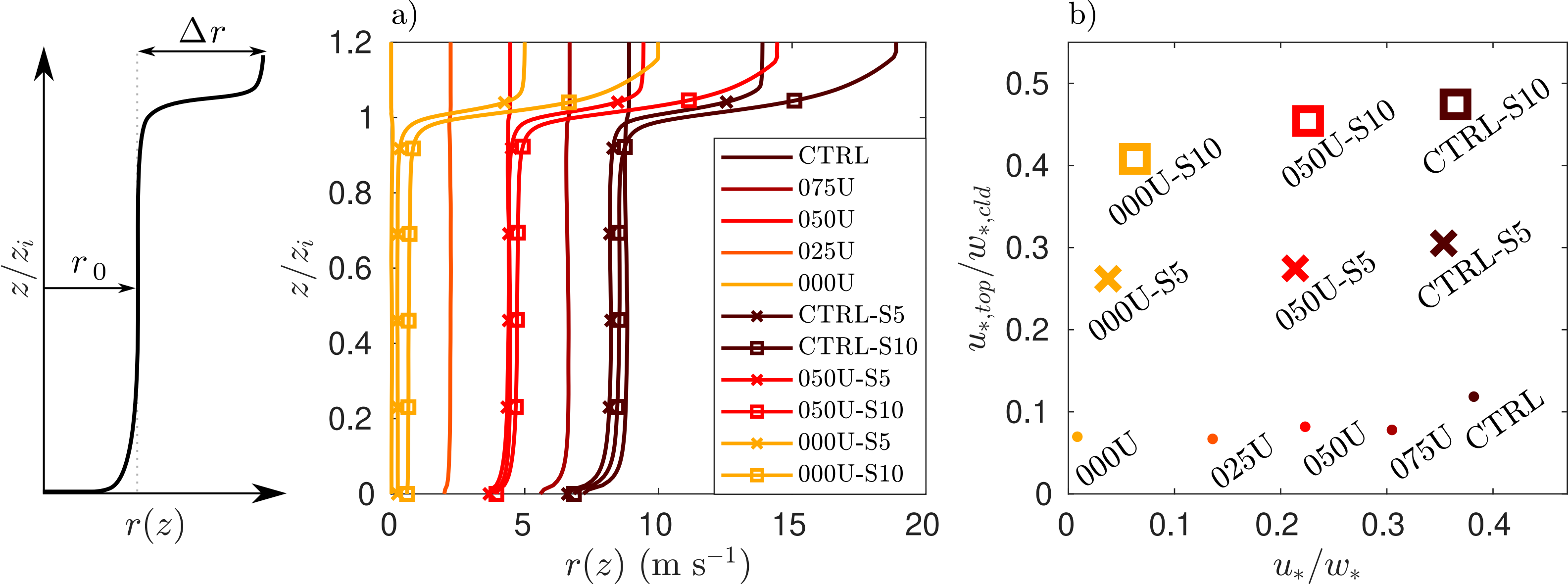
a)
b)
Δr
r_0
z/z_i
$r(z)$
$r(z)$ (m s^{-1})
$u_{*,top}/w_{*,cld}$
u_*/w_*
CTRL
075U
050U
025U
000U
CTRL-S5
CTRL-S10
050U-S5
050U-S10
000U-S5
000U-S10

Figure 2.

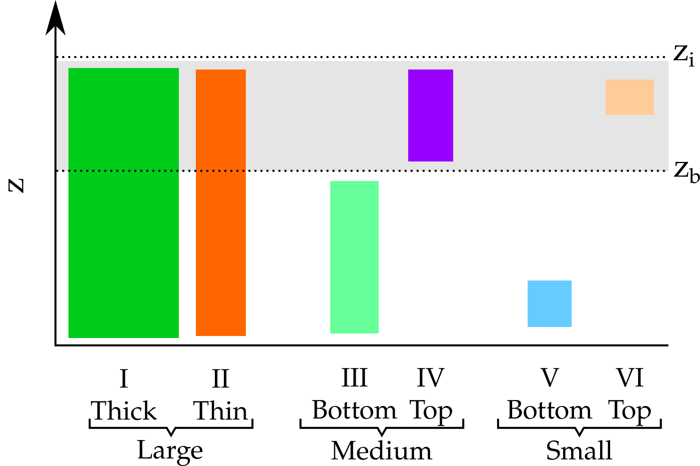
z
z_i
z_b
I
Thick
II
Thin
Large
III
Bottom
IV
Top
Medium
V
Bottom
VI
Top
Small

Figure 3.

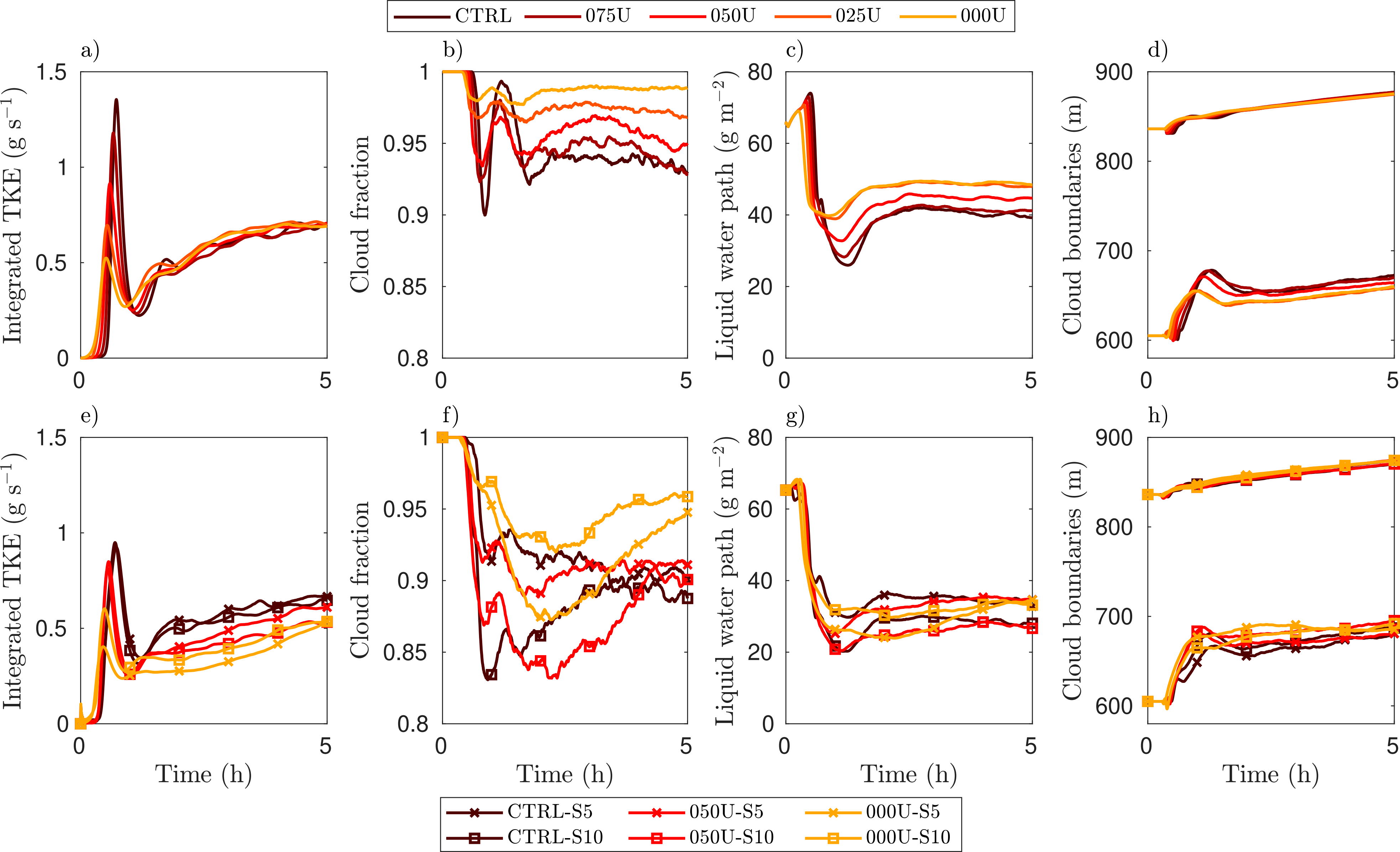

CTRL
075U
050U
025U
000U
a)
b)
c)
d)
e)
f)
g)
h)
Integrated TKE (g s^{-1})
Cloud fraction
Liquid water path (g m^{-2})
Cloud boundaries (m)
Time (h)
1.5
1
0.5
0
0.95
0.9
0.85
0.8
80
60
40
20
900
800
700
600
5
CTRL-S5
CTRL-S10
050U-S5
050U-S10
000U-S5
000U-S10

Figure 4.

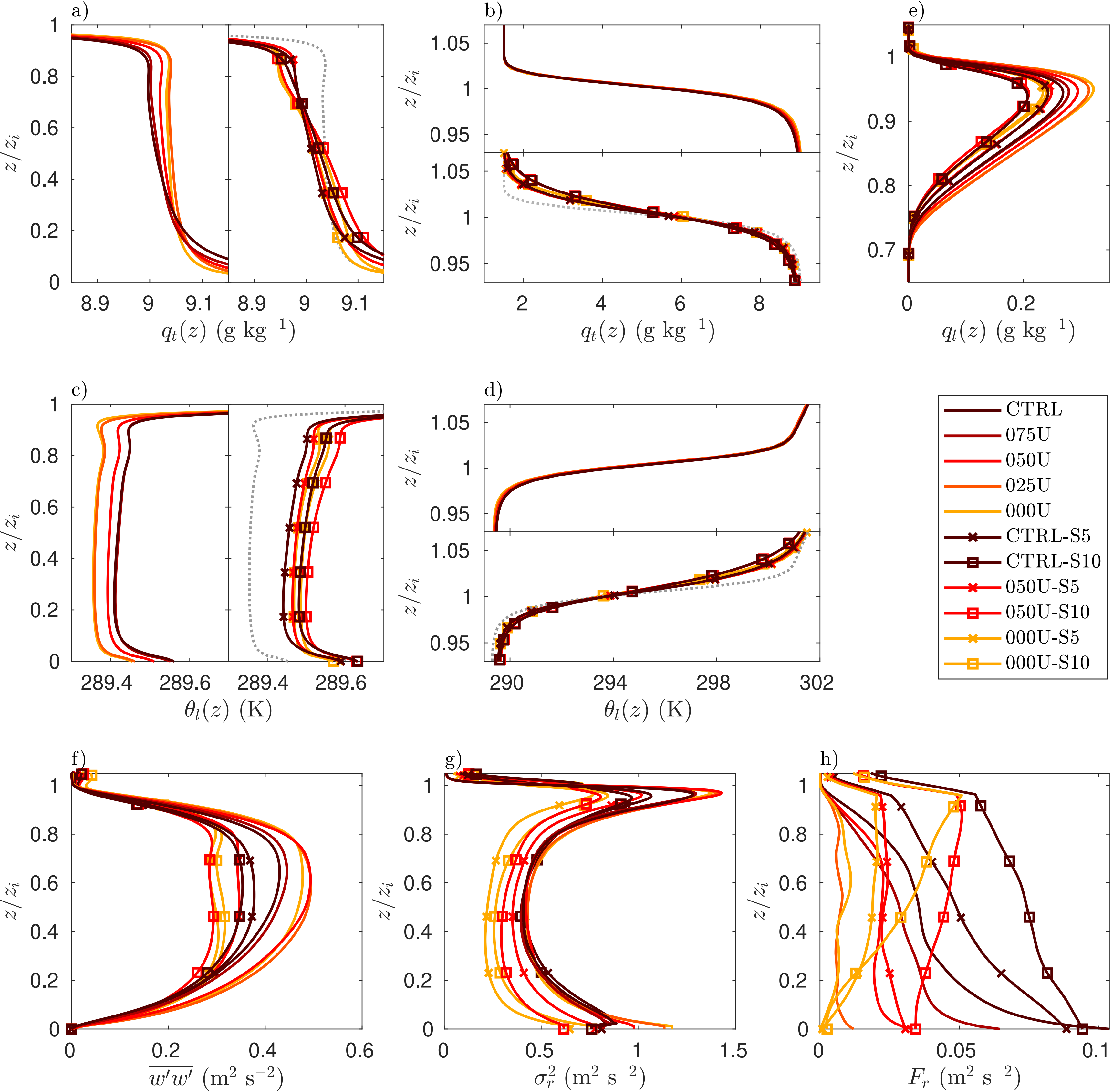
a)
b)
e)
c)
d)
f)
g)
h)
z/z_i
$q_t(z)$ (g kg^{-1})
$q_l(z)$ (g kg^{-1})
$\theta_l(z)$ (K)
$\overline{w'w'}$ (m^2 s^{-2})
σ_r^2 (m^2 s^{-2})
F_r (m^2 s^{-2})
CTRL
075U
050U
025U
000U
CTRL-S5
CTRL-S10
050U-S5
050U-S10
000U-S5
000U-S10

Figure 5.

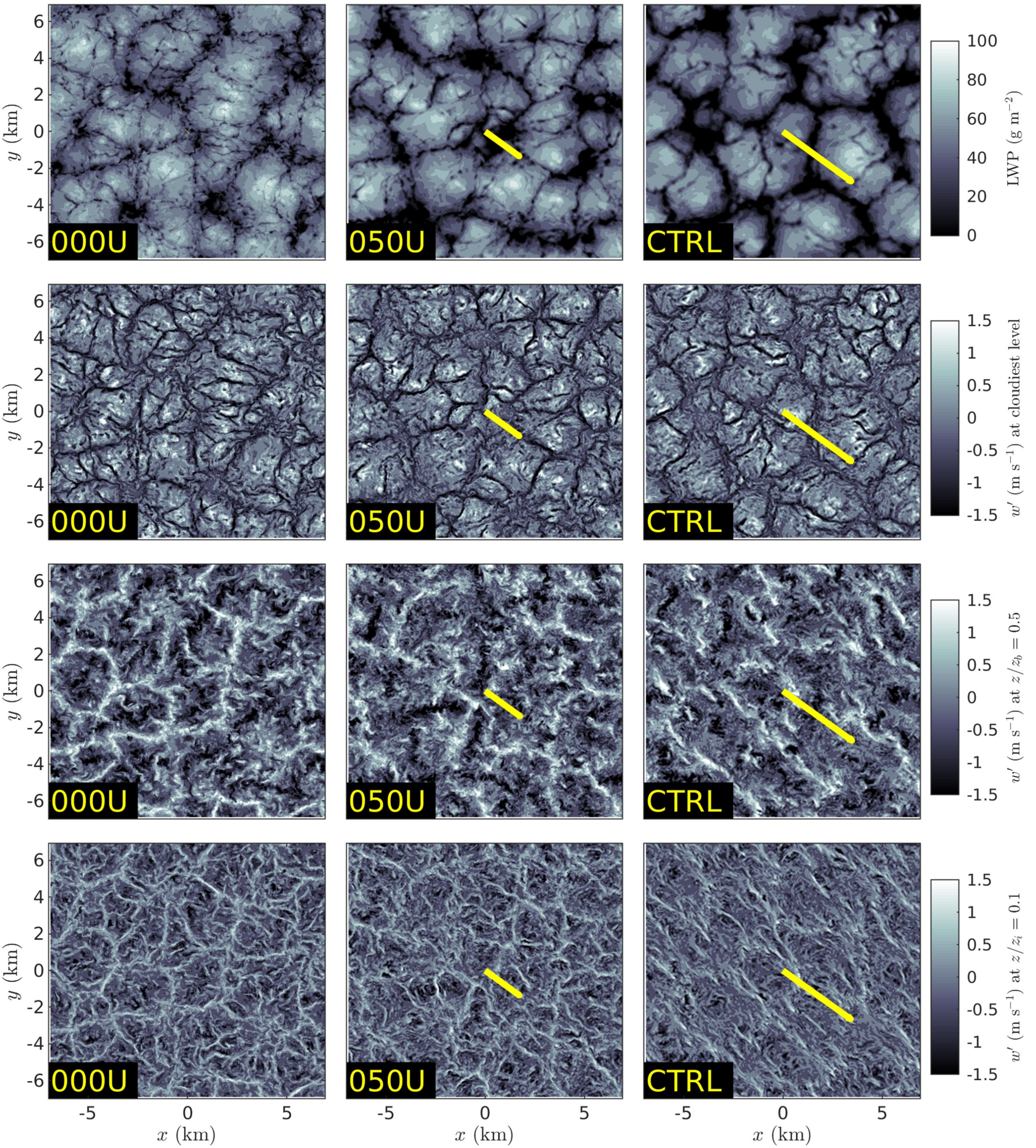
000U
050U
CTRL
y (km)
x (km)
LWP (g m^{-2})
w' (m s^{-1}) at cloudiest level
w' (m s^{-1}) at $z/z_b = 0.5$
w' (m s^{-1}) at $z/z_i = 0.1$

Figure 6.

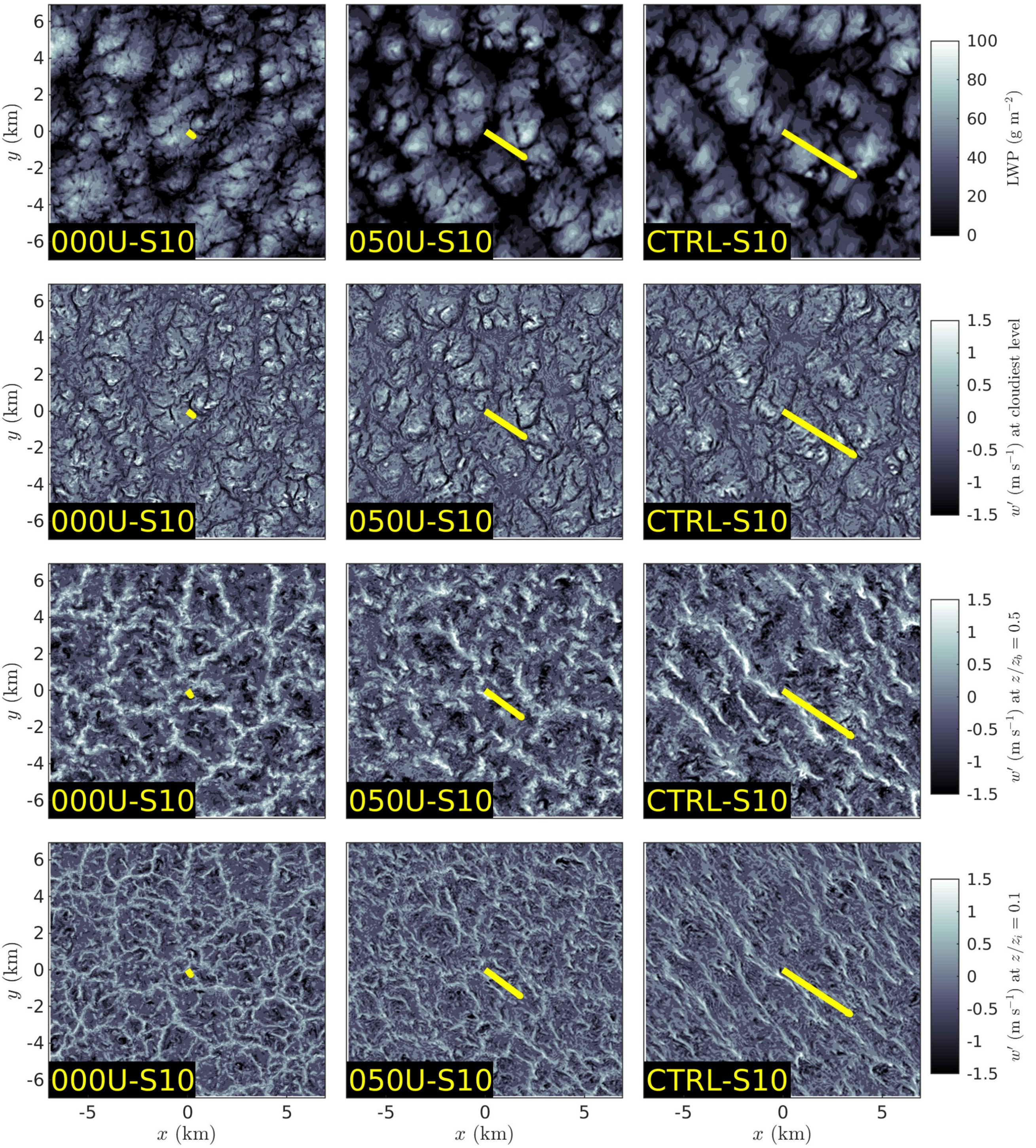
000U-S10
050U-S10
CTRL-S10
y (km)
x (km)
LWP (g m^{-2})
w' (m s^{-1}) at cloudiest level
w' (m s^{-1}) at $z/z_b = 0.5$
w' (m s^{-1}) at $z/z_i = 0.1$

Figure 7.

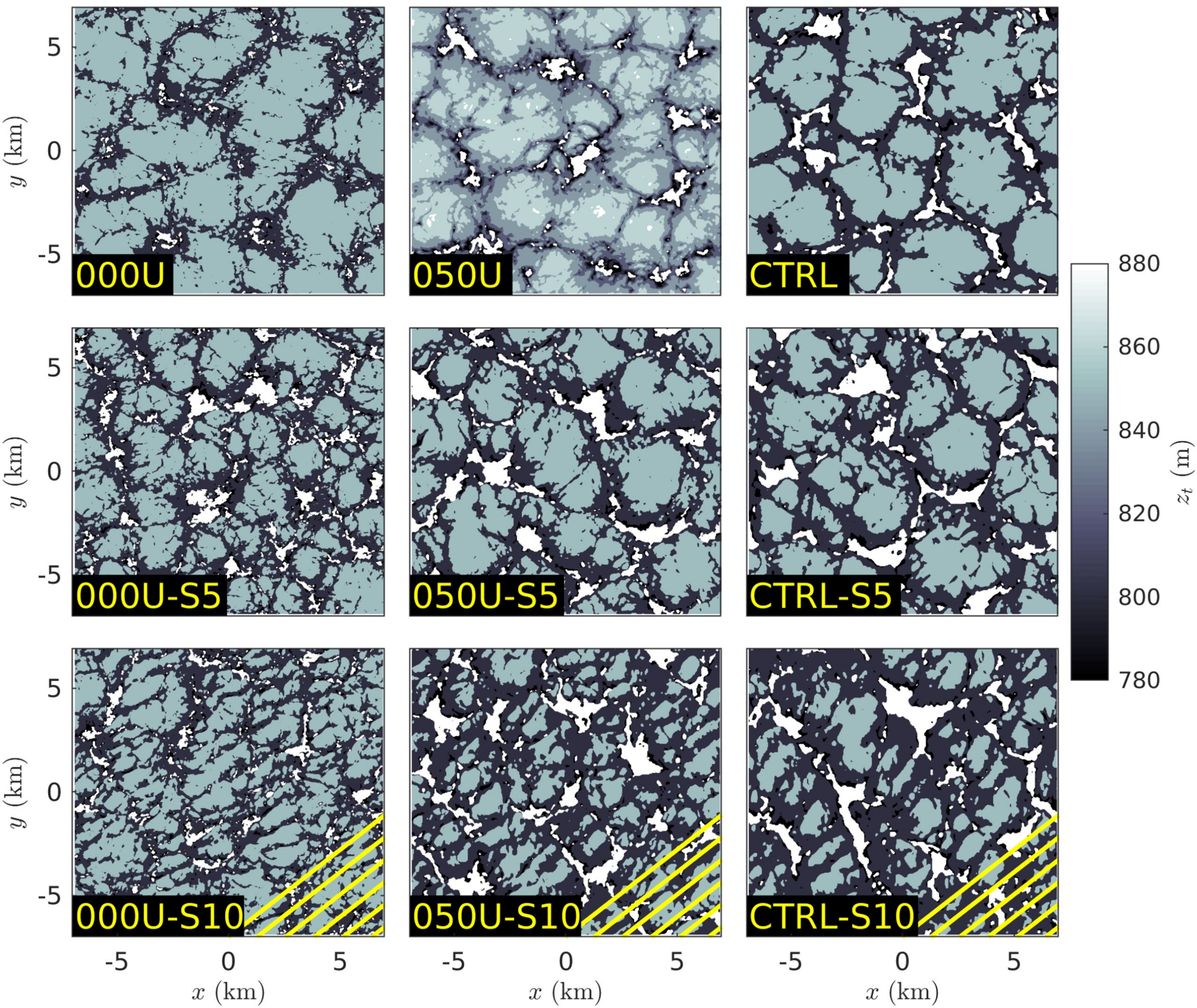
000U
050U
CTRL
000U-S5
050U-S5
CTRL-S5
000U-S10
050U-S10
CTRL-S10
y (km)
x (km)
z_t (m)
880
860
840
820
800
780
5
0
-5

Figure 8.

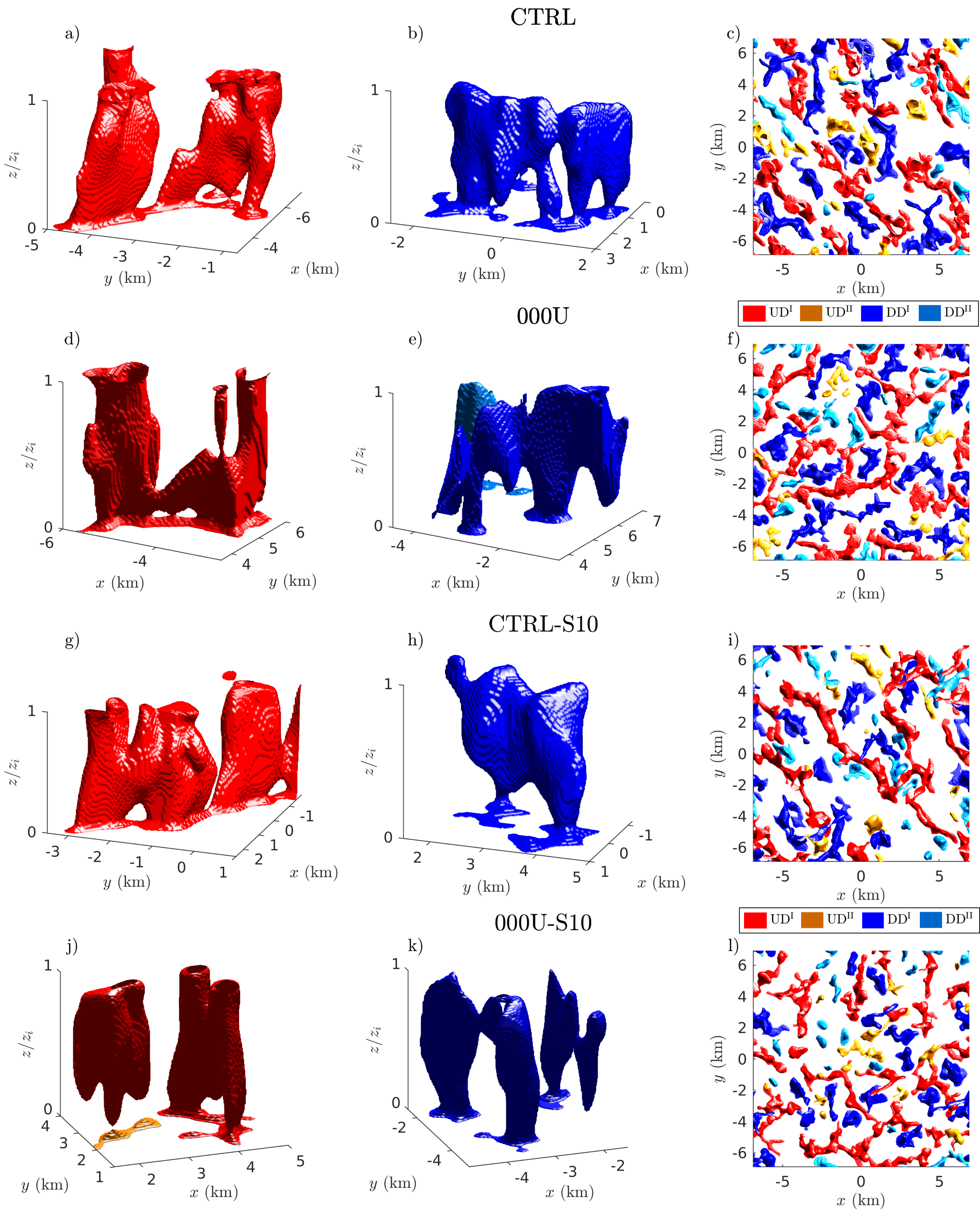

CTRL
a)
b)
c)
000U
d)
e)
f)
CTRL-S10
g)
h)
i)
000U-S10
j)
k)
l)
z/z_i
x (km)
y (km)
$\mathrm{UD^I}$
$\mathrm{UD^{II}}$
$\mathrm{DD^I}$
$\mathrm{DD^{II}}$

Figure 9.

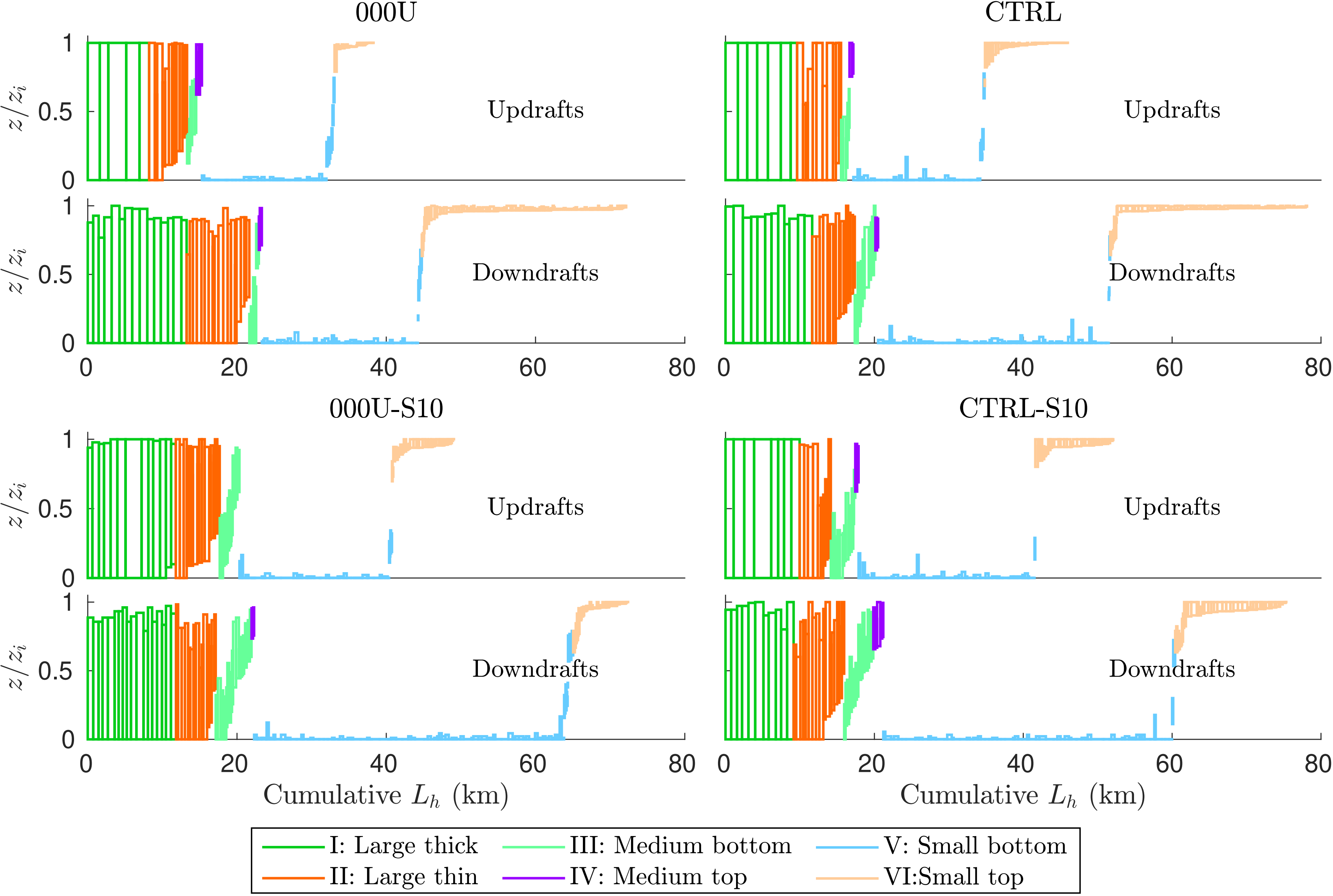
000U
CTRL
000U-S10
CTRL-S10
Updrafts
Downdrafts
z/z_i
Cumulative L_h (km)
I: Large thick
II: Large thin
III: Medium bottom
IV: Medium top
V: Small bottom
VI:Small top

Figure 10.

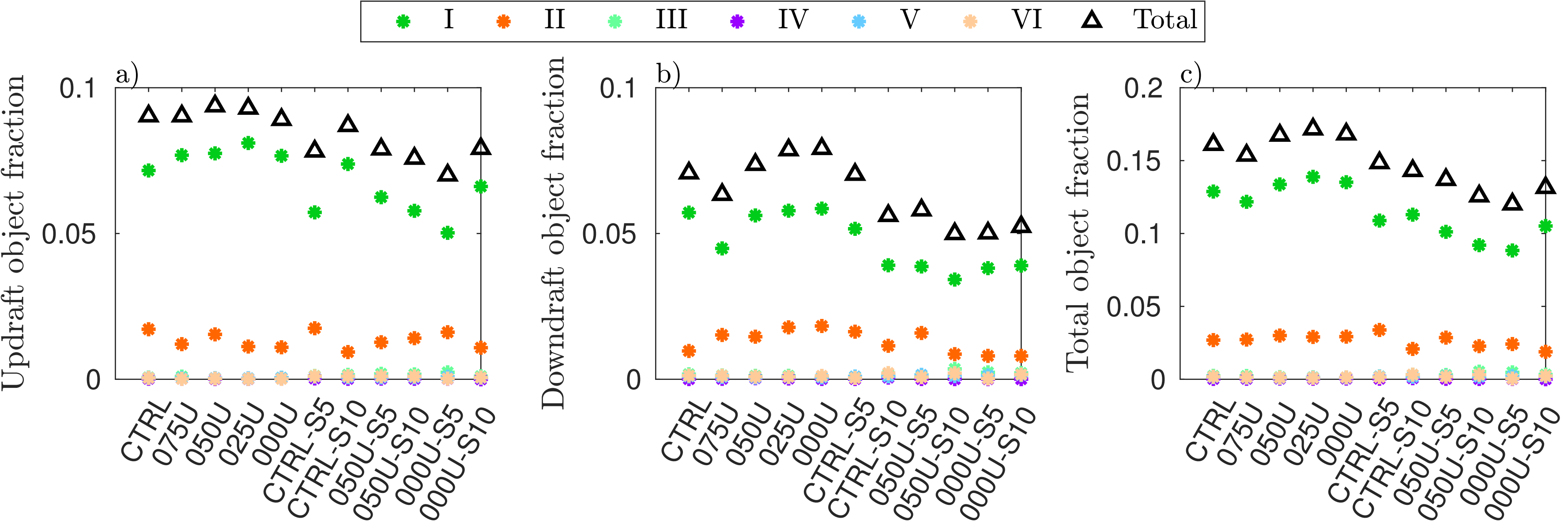

I
II
III
IV
V
VI
Total
a)
b)
c)
Updraft object fraction
Downdraft object fraction
Total object fraction
0
0.05
0.1
0.15
0.2
CTRL
075U
050U
025U
000U
CTRL-S5
CTRL-S10
050U-S5
050U-S10
000U-S5
000U-S10

Figure 11.

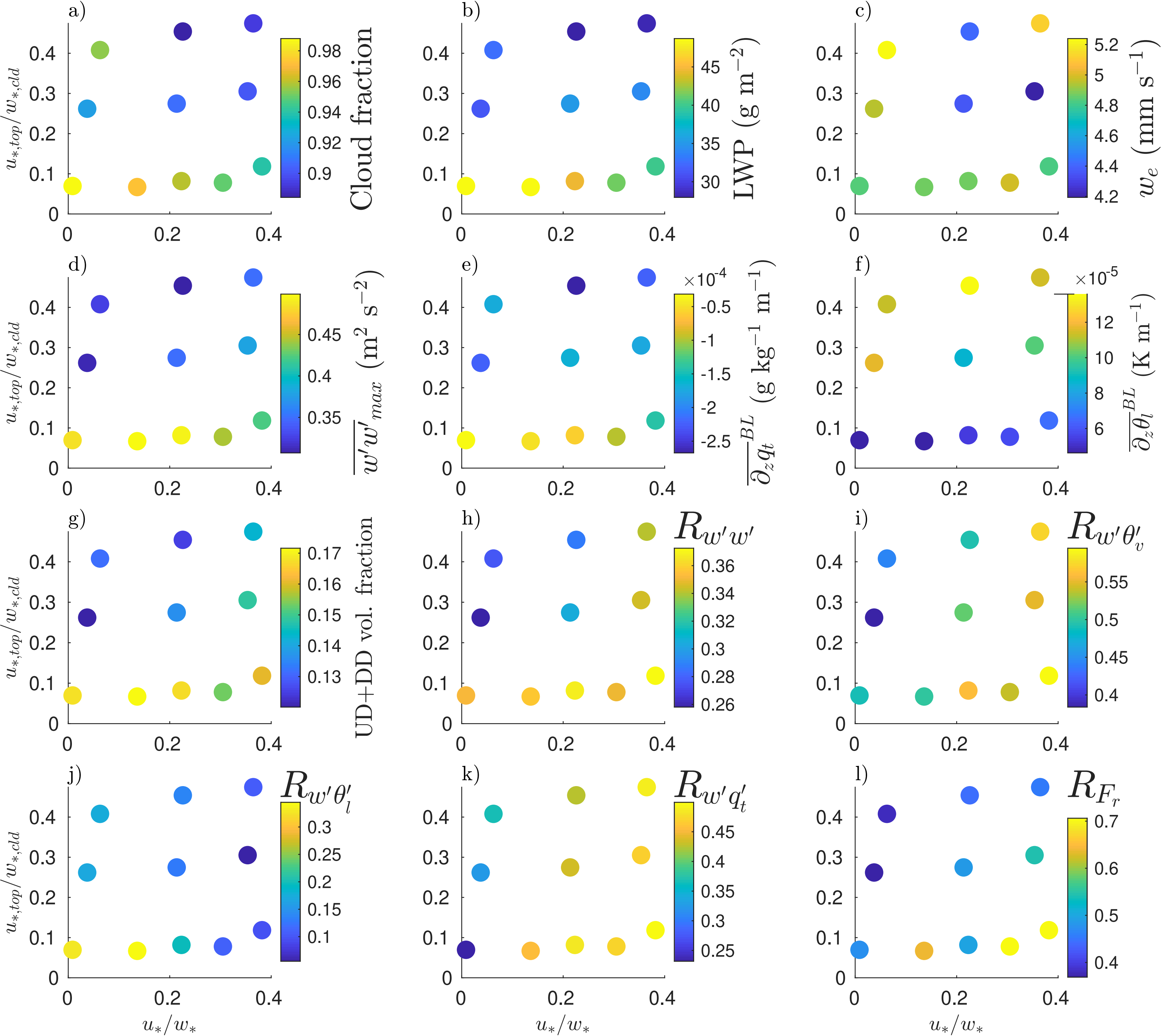

a)
Cloud fraction
b)
LWP (g m^{-2})
c)
w_e (mm s^{-1})
d)
$\overline{w'w'}_{max}$ (m^2 s^{-2})
e)
$\overline{\partial_z q_t}^{BL}$ (g kg^{-1} m^{-1})
×10^{-4}
f)
$\overline{\partial_z \theta_l}^{BL}$ (K m^{-1})
×10^{-5}
g)
UD+DD vol. fraction
h)
$R_{w'w'}$
i)
$R_{w'\theta_v'}$
j)
$R_{w'\theta_l'}$
k)
$R_{w'q_t'}$
l)
R_{F_r}
$u_{*,top}/w_{*,cld}$
u_*/w_*

Figure 12.

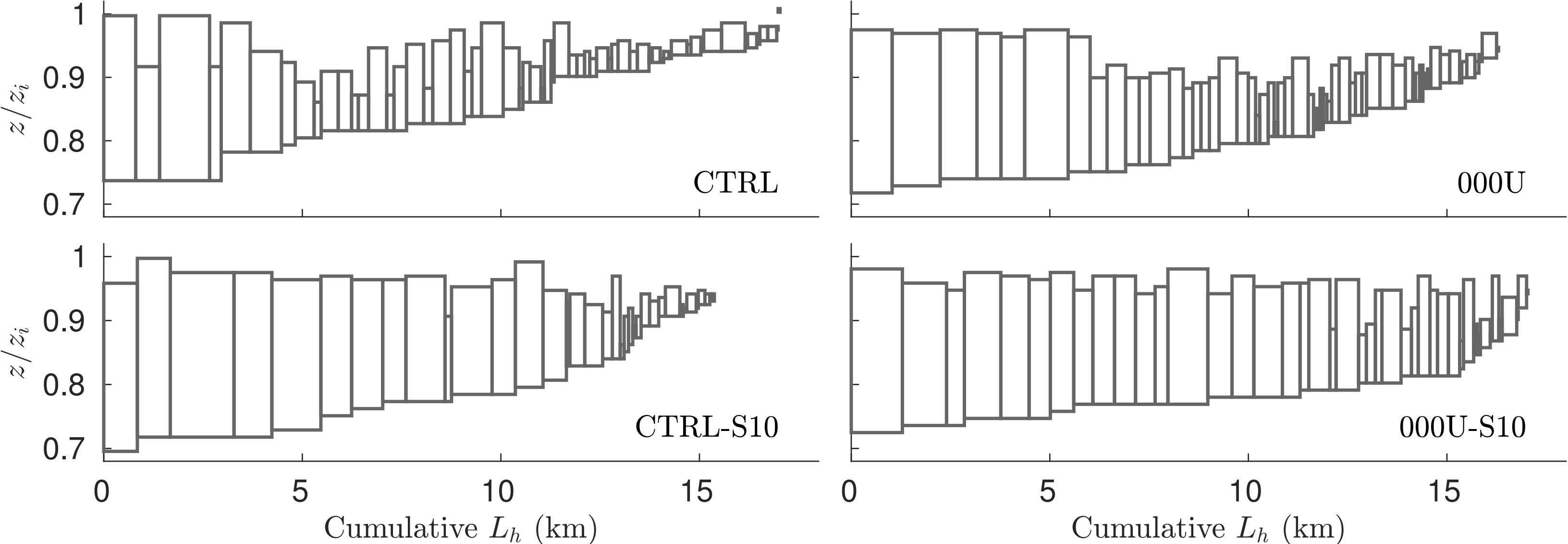

CTRL
000U
CTRL-S10
000U-S10
z/z_i
Cumulative L_h (km)

Figure 13.

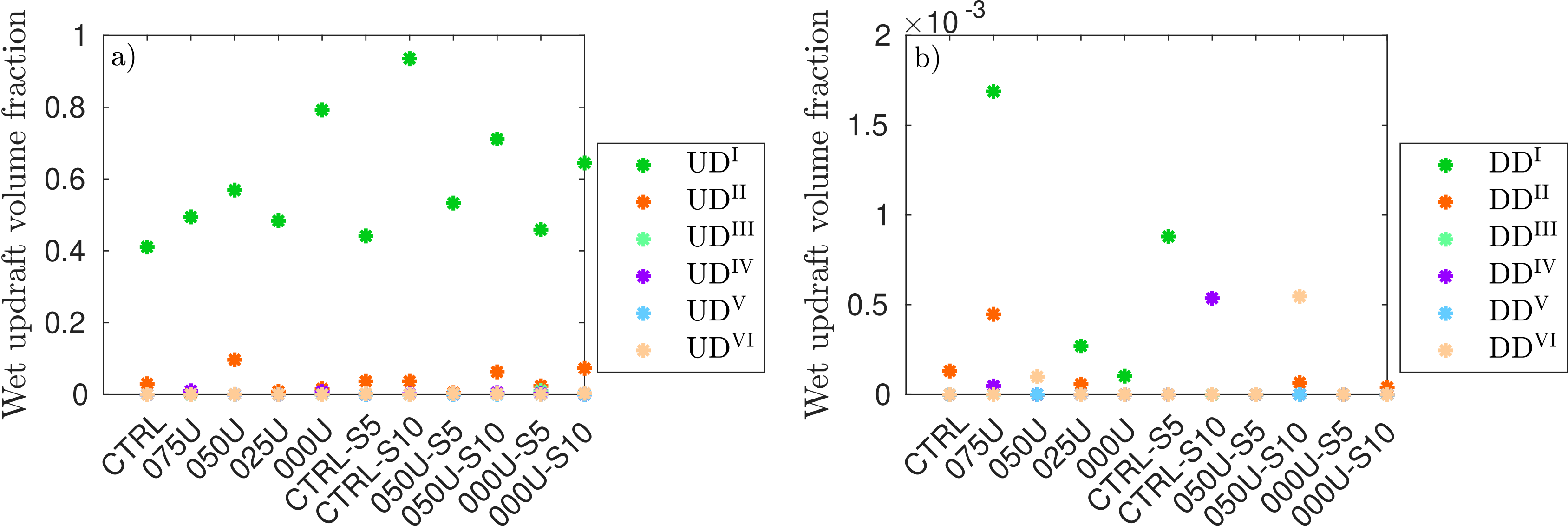
a)
Wet updraft volume fraction
0
0.2
0.4
0.6
0.8
1
CTRL
075U
050U
025U
000U
CTRL-S5
CTRL-S10
050U-S5
050U-S10
000U-S5
000U-S10
UD^{I}
UD^{II}
UD^{III}
UD^{IV}
UD^{V}
UD^{VI}
b)
$\times 10^{-3}$
Wet updraft volume fraction
0
0.5
1
1.5
2
DD^{I}
DD^{II}
DD^{III}
DD^{IV}
DD^{V}
DD^{VI}